International Journal of Architectural Heritage
Conservation, Analysis, and Restoration

ISSN: 1558-3058 (Print) 1558-3066 (Online) Journal homepage: www.tandfonline.com/journals/uarc20

Block-Based Simulation of the Out-of-Plane Seismic Response of Non-Framed Unreinforced Masonry Walls with Pre-Existing Settlement-Induced Damage

Amirhossein Ghezelbash , Alfonso Prosperi , Satyadhrik Sharma , Antonio Maria D'Altri , Jan G. Rots & Francesco Messali

To cite this article: Amirhossein Ghezelbash , Alfonso Prosperi , Satyadhrik Sharma , Antonio Maria D'Altri , Jan G. Rots & Francesco Messali (24 Apr 2026): Block-Based Simulation of the Out-of-Plane Seismic Response of Non-Framed Unreinforced Masonry Walls with Pre-Existing Settlement-Induced Damage, International Journal of Architectural Heritage, DOI: 10.1080/15583058.2026.2663125

To link to this article: https://doi.org/10.1080/15583058.2026.2663125

INTERNATIONAL JOURNAL OF ARCHITECTURAL HERITAGE
https://doi.org/10.1080/15583058.2026.2663125

Taylor & Francis
by informa

RESEARCH ARTICLE

OPEN ACCESS Check for updates

Block-Based Simulation of the Out-of-Plane Seismic Response of Non-Framed Unreinforced Masonry Walls with Pre-Existing Settlement-Induced Damage

Amirhossein Ghezelbash[a], Alfonso Prosperi[b], Satyadhrik Sharma[c], Antonio Maria D'Altri[d], Jan G. Rots[a], and Francesco Messali[a]

[a]Faculty of Civil Engineering and Geosciences, Delft University of Technology, Delft, The Netherlands; [b]Department of Building Materials & Structures, The Netherlands Organization for Applied Scientific Research (TNO), Delft, The Netherlands; [c]Reliable Structures Section, The Netherlands Organization for Applied Scientific Research (TNO), Delft, The Netherland; [d]Department of Civil, Chemical, Environmental, and Materials Engineering, University of Bologna, Bologna, Italy

ABSTRACT

This paper presents a numerical investigation on the effects of settlement-induced pre-damage on the seismic out-of-plane (OOP) response of two-way spanning non-framed unreinforced masonry (URM) walls, investigating also the suitability of static analysis procedures for simulating the dynamic OOP response of pre-damaged walls. For this purpose, the finite-element block-based modeling approach developed and validated by the authors in previous works is employed. URM walls with various geometries and boundary conditions are simulated to investigate the effects of openings and wall-to-diaphragm connections on pre-damage effects. Each specimen is subjected to various settlement profiles, and different levels of obtained settlement-induced damage states are used as initial conditions for OOP analyses. Static and dynamic OOP simulations, the latter considering both induced and tectonic seismicity, and modal analyses are performed. The outputs show that settlement effects on the OOP response emerged as early as the light pre-damage state. Sagging, previously considered in literature less damaging than hogging, caused the greatest OOP stiffness and strength reduction, up to 92% and 80%, respectively. Hogging led to a 60% stiffness and 30% strength drop, particularly in walls with openings. Induced seismicity did not lead to collapse. Static analyses accurately estimated OOP strength and failure mechanisms.

ARTICLE HISTORY
Received 6 March 2026
Accepted 16 April 2026

KEYWORDS
Numerical modeling; out-of-plane; seismic loading; settlement damage; unreinforced masonry

1. Introduction

URM is a composite material consisting of bricks, blocks, or stones connected together with mortar. URM is widely used in construction globally, forming a major part of both historical buildings and modern low-rise structures (Hendry 2001). In Netherlands, over 90% of residential buildings are made using brick URM (Billio et al. 2022). The popularity of URM stems from its ease of construction, low costs, good acoustic and thermal insulation, and minimal maintenance requirements (Bojadjiev et al. 2025). The high compressive strength of URM allows it to perform well under gravity loads, making URM walls suitable for vertical load-bearing in non-framed constructions (Soundar Rajan and Jegatheeswaran 2023). However, URM buildings are known to perform poorly under lateral loads such as earthquakes, flooding, or impact, due to their low tensile and shear resistance (D'Ayala and Paganoni 2011; Moon et al. 2014; Oyarzo-Vera and Griffith 2009; Page 1991; Penna et al. 2014). These lateral forces may act in-plane (IP) or out-of-plane (OOP) of the walls, and URM buildings are particularly weak against the latter (Furtado et al. 2018; Pradhan et al. 2021). OOP failure of URM walls in non-framed buildings often leads to complete collapse (Dolatshahi and Aref 2016), highlighting the need for further research to improve understanding of OOP responses.

Some URM structures have not been designed with engineered resistance to seismic loads (Korany, Drysdale, and Chidiac 2001). Hence, their seismic vulnerability is even more poorly understood. In addition, URM buildings may have accumulated damage from past loadings, further increasing their vulnerability to new seismic loads. The building stock in the Groningen province in Netherlands presents a clear example. In this region, repeated earthquakes induced by gas extraction, and the occurrence of subsidence processes, have damaged URM buildings for decades (van Staalduinen Pc, Terwel, and Rots 2018). Though low in magnitude, about 1700 events have occurred to date, raising seismic risks in an area not known for tectonic activity (Busscher and Vojvodić

CONTACT Amirhossein Ghezelbash a.ghezelbash@tudelft.nl Faculty of Civil Engineering and Geosciences, Delft University of Technology, Stevinweg 1, Delft 2628 CN, The Netherlands

2025). Around 28,000 residential URM buildings are affected by these conditions (van Staalduinen Pc, Terwel, and Rots 2018). The situation is worsened by two key issues: the high (height-to-thickness) slenderness of walls reducing their OOP strength and long-term ground settlement causing pre-existing structural damage (Prosperi 2025). Ground settlement refers to the vertical displacement of the ground surface (Bucx et al. 2015), resulting from both natural phenomena and human-induced activities such as construction, mining, excavation, and tunneling (Peduto et al. 2022; Peduto, Ferlisi, et al. 2017; Saeidi, Deck, and Verdel 2009; Stouthamer et al. 2020). It poses a significant issue in regions prone to subsidence, particularly those underlain by soft soils (Koster, Stafleu, and Stouthamer 2018; Nieuwenhuis and Schokking 1997; van Asselen et al. 2018). When subsidence occurs unevenly, it leads to differential settlements, which can cause structural issues such as sinking, tilting, or cracking (Costa, Kok, and Korff 2020; Nicodemo, Peduto, and Ferlisi 2020; Peduto et al. 2016, 2019; Peduto, Nicodemo, et al. 2017). In the Netherlands, URM buildings, such as those in Groningen, are particularly vulnerable to settlement and vibrations due to the quasi-brittle nature of their construction materials and the common use of shallow foundation systems (Prosperi 2025). In other words, buildings face seismic loads they are not designed to resist, while already weakened. Financial consequences are severe, with €10 billion already spent on repairs and another €12 billion expected for future reinforcements and homeowner compensation (Busscher and Vojvodić 2025). In addition, about 29% of the population in the region reports feeling unsafe in their homes (Boelhouwer and van der Heijden 2018), demonstrating the broad societal impact of the situation.

Extensive efforts have been made to reduce the risk of damage and collapse in URM building stock of Groningen (Maatschappelijke Effecten Inventarisatie van Aardbevingen in Noordoost Groningen 2016; Messali, Rots, and Walraven 2020). These efforts involve assessing buildings in their current condition and designing strengthening solutions to improve earthquake resilience. However, most current assessment techniques assume URM buildings are in pristine condition (Gentile et al. 2022), which does not reflect the reality of the Groningen case. Research has moved in two main directions to tackle this limitation: one aims to measure the level of existing damage through visual crack evaluation, and the other explores how this damage affects seismic performance. The problem lies in the imbalance between these areas. While methods for quantifying damage have advanced (Korswagen 2024), little research has studied how such damage impacts seismic response. Only a few studies examine the effects of pre-damage on seismic response due to the complexities of physical testing (Beyer 2012; Bui et al. 2017; Dalgic et al. 2023; Giardina et al. 2012; Karanikoloudis, Serra, and Lourenço 2024; Meoni et al. 2025; F. Portioli and Cascini 2017; Son and Cording 2005) and the unavailability of reliable numerical modeling tools (Korany, Drysdale, and Chidiac 2001). Moreover, only one study has preliminarily investigated the effects of settlement-induced pre-damage (Korswagen et al. 2024). However, this contribution studies the IP performance of pre-damaged specimens and not their more vulnerable OOP performance. This creates a significant gap in understanding and preparedness.

The current study aims to contribute to the ongoing efforts to mitigate the risk of structural collapse in Groningen. This objective is pursued through a numerical investigation of the effects of settlement-induced pre-damage on the seismic OOP response of non-framed URM walls. For this purpose, the modeling approach developed by the authors in (D'Altri et al. 2019) and extended in (Ghezelbash, D'Altri, et al. 2025; Ghezelbash, Sharma, et al. 2025) for the dynamic simulation of one- and two-way spanning URM walls under seismic loading is employed. The approach simulates URM unit-by-unit via nonlinear expanded blocks and cohesive frictional zero-thickness joints. It has been successfully used in previous studies for the prediction and assessment of complex OOP responses (Ghezelbash, Aşıkoğlu, et al. 2025; Ghezelbash, D'Altri, et al. 2026; Ghezelbash, Sharma, et al. 2025), yielding reliable outcomes consistent with real-world responses. It is favored over the conventionally used continuum-based (Burd et al. 2000, 2022; Giardina et al. 2013; Korswagen et al. 2024; Longo et al. 2021; Netzel 2009; Peduto et al. 2022; Prosperi et al. 2023a, 2023b; Rots, Korswagen, and Longo 2021; Yiu, Burd, and Martin 2018) or macro-elements-based (Ferlisi et al. 2020; Nicodemo, Peduto, and Ferlisi 2019) approaches typically adopted to study settlement damage as it provides more detailed insights into both global and local responses (D'Altri et al. 2020). Furthermore, unlike other detailed block-based approaches currently employed in the literature to investigate settlement effects, it does not rely on simplifying assumptions such as simulating dry-joint specimens (Bui et al. 2017; Gagliardo et al. 2021; F. Portioli and Cascini 2017; F. P. A. Portioli et al. 2023) or modeling 2D façades (X. Chen et al. 2021; D'Altri et al. 2025; Hong and Laefer 2008; Son and Cording 2005, 2007), which neglect the contribution of adjacent walls to the OOP response of the specimen under study. Additionally, the modeling approach used in this study has already been validated against wall experiments with multi-step sequences of dynamic OOP loading (Ghezelbash, D'Altri, et al. 2025; Ghezelbash, Sharma, et al. 2025), demonstrating very good performance in capturing the effects of progressive damage in the subsequent OOP responses up to collapse. Therefore, the

capability of the approach to capture the effect of pre-damage on OOP performance is already proven.

The study is presented as follows. Section 2 summarizes the key features of the modeling approach, including geometrical representation, material characterization, numerical solution, and energy dissipation procedures. In Section 3, the ability of the approach to model settlement-induced damage is validated through simulating several wallet- to wall-level experiments. Afterwards, the setup of the parametric analysis conducted to investigate the OOP performance of walls pre-damaged by settlement is outlined in Section 4, along with comments on the limitations of the study. In summary, several two-way-spanning walls with varying boundary conditions and opening configurations are considered. The specimens are subjected to different settlement profiles, and various damage states are identified during their response. These damage states are then used as initial conditions for subsequent OOP loading. OOP analyses are performed in both static and dynamic regimes to assess the suitability of the former as a simplified alternative for studying seismic OOP response of pre-damaged walls. Two types of dynamic signals are considered, one from an induced-seismicity event and one from a tectonic earthquake, to compare interaction effects under both hazards. The results of the parametric analysis are presented in Section 5 in terms of the different types of settlement-induced pre-damage patterns observed in each specimen and loading scenario, and their effect on OOP stiffness, static (pushover) OOP strength, and dynamic OOP collapse of the specimens. The main outcomes of the study are ultimately presented in Section 0 with suggestions for future research.

2. Numerical modeling approach

This study uses the high-fidelity block-based numerical approach developed in (D'Altri et al. 2019) for modeling the quasi-static material- to building-level responses of URM, and extended to dynamic simulations in (Ghezelbash, D'Altri, et al. 2025). The approach falls within the category of simplified micro-scale modeling techniques, such as those developed in (D'Altri et al. 2018; Furiosi et al. 2025; Kesavan and Menon 2022; Macorini and Izzuddin 2011; Malomo, Pinho, and Penna 2020; Mohyeddin, Goldsworthy, and Gad 2013; Nie et al. 2023; Oktiovan, Davis, et al. 2024; Oktiovan, Messali, et al. 2024; Xie et al. 2021), and is well suited for the detailed investigation of both local and global responses of URM structures under various actions, including seismic loading. As the approach has been extensively described in previous publications of the authors (Ghezelbash, D'Altri, et al. 2025, 2026; Ghezelbash, Messali, and Rots 2023a), only a summary of its key features is provided herein.

2.1. Geometrical representation

The approach employs expanded blocks to represent the masonry units and idealizes the mortar layers as zero-thickness horizontal (bed) and vertical (head) joints, as shown in Figure 1a. The expanded blocks are dimensioned to match the unit size plus one mortar thickness in both the length and height directions. Each block is discretized into a $4 \times 2 \times 2$ (length × height×thickness) array of eight-node hexahedral finite elements. The zero-thickness joints are implemented using a node-to-surface contact algorithm (Weyler et al. 2012), where contact is established at discrete points by associating each point on one surface (shown as purple circles in the figure) with multiple points on the opposing surface (represented by pink surfaces in the figure). These contact points correspond to the external nodes of the meshed expanded blocks. The previous studies of the authors (Ghezelbash et al. 2024; Ghezelbash, Aşıkoğlu, et al. 2026; Ghezelbash, D'Altri, et al. 2025; Ghezelbash, Sharma, et al. 2025) have shown that the adopted discretization of the expanded blocks, combined with three contact points across the thickness of the joints, is sufficient to simulate material- to wall-level responses realistically and accurately, while maintaining optimized computational demands.

2.2. Mechanical assumptions

The expanded blocks behave nonlinearly and can represent the compressive failure of URM assemblies and the tensile cracking of URM units, as illustrated in Figure 1(b). Their nonlinear behavior is modeled using the isotropic constitutive model known as Concrete Damaged Plasticity (CDP) (Lubliner et al. 1989), which employs a Drucker-Prager type multi-yield surface (Lee and Fenves 1998) to identify the onset of nonlinearity. The compressive behavior of the expanded blocks includes an initial elastic phase, followed by a plateau, and then a linear softening branch. In tension, the behavior is defined by an elastic regime followed by linear softening. To prevent numerical instability during large nonlinearities and deformations, 10% residual strength is maintained in the post-softening regime for both tension and compression. The cyclic behavior of the expanded blocks includes elastic unloading within the elastic regimes and the compressive plateau, and reduced-stiffness unloading during the softening phase, with the slope of unloading proportional to the loss of strength. The tensile and compressive behaviors

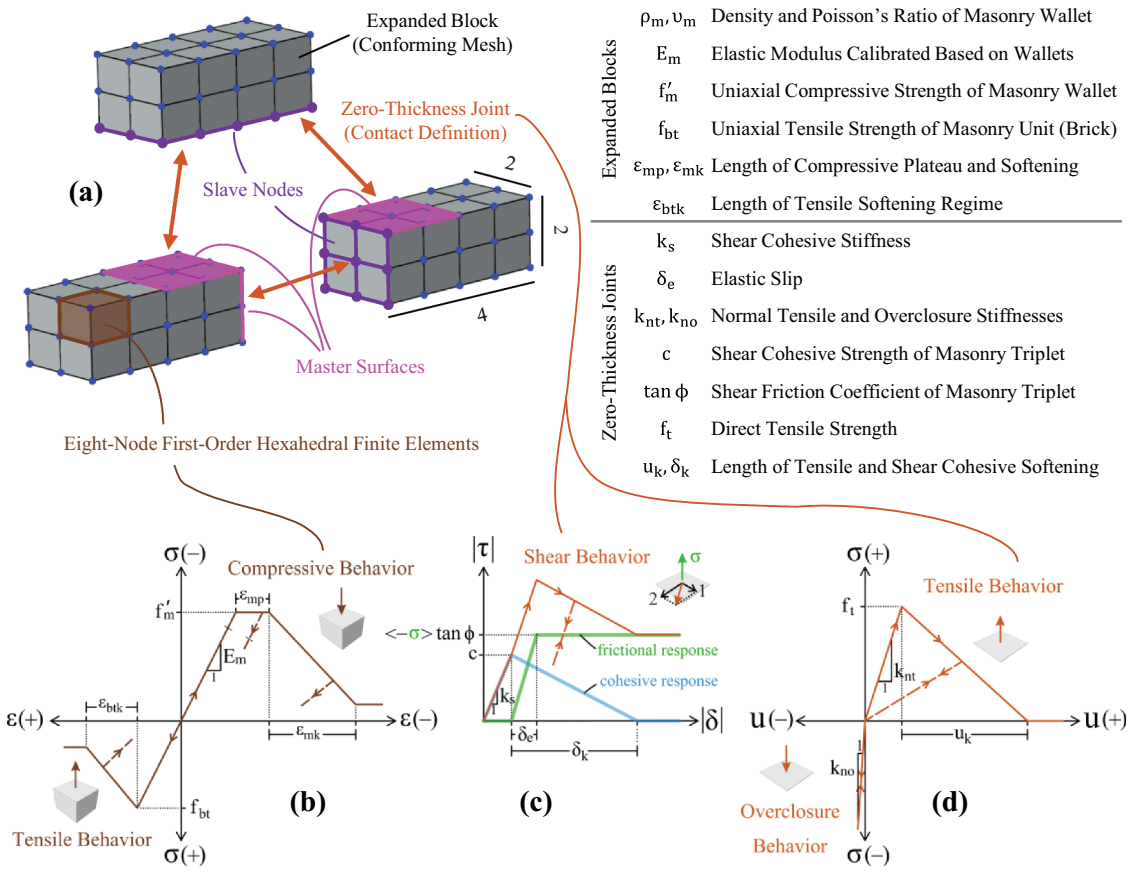

Figure 1. Visual summary of the numerical modeling approach used in this study: geometrical representation of URM (a), compressive and tensile behavior of the expanded blocks (b), tangential shear response of the zero-thickness joints (c), and their normal tensile and overclosure responses (d). The shear response of the joints is drawn for a scenario where $\langle -\sigma \rangle \tan \phi$ is larger than c, and elastic slip is steeper than cohesive stiffness.

are coupled, such that softening in one leads to a proportional strength reduction in the other.

The zero-thickness joints behave nonlinearly in both tangential and normal directions, representing the shear and tensile failure of the mortar layer and the mortar-unit bond interface, respectively. Their nonlinear behavior evolves based on the relative displacement of the contact nodes and employs a finite-sliding formulation, enabling the simulation of large separations, sliding, and rotations of the surfaces (Hibbitt, Karlsson, and Sorensen 2011). In the tangential direction, the joints exhibit an isotropic cohesive-frictional shear behavior, as illustrated in Figure 1c. The cohesive component consists of an initial elastic branch followed by linear softening. The frictional component initiates at the onset of cohesive softening and includes an initial elastic slip phase followed by a regime of constant friction. The normal tensile behavior of the joints, shown in Figure 1d, is purely cohesive, characterized by an elastic regime followed by linear softening. In both shear and tensile responses, the softening progresses to a zero-strength state. The cohesive shear and tensile behaviors are coupled, such that softening in one causes proportional softening in the other. Under cyclic loading, the cohesive behaviors follow secant unloading, while the frictional behavior unloads elastically. The normal overclosure behavior is elastic, with a high stiffness to prevent significant interpenetration of the blocks. Finally, the joints are modeled as non-dilatant, with dilatancy effects considered in the behavior of the expanded blocks.

2.3. Solution procedure

The modeling approach employs an implicit-based static solution procedure for the simulation of gravity, vertical, and quasi-static loading (D'Altri et al. 2019). For dynamic analyses, it utilizes the Hilber-Hughes-Taylor-α (HHT-α) direct integration implicit solver (Hilber, Hughes, and Talor 1977), with minimal numerical damping. Both solvers operate with automatic stepping, referred to as load increment stepping in the static solver and time-stepping in the dynamic solver. This automatic stepping enables efficient progression of the

analyses: large increments are used when the specimen exhibits low nonlinearity, while smaller step sizes are adopted during highly nonlinear phases requiring a larger number of iterations. This adaptability mitigates the risk of numerical instability. To prevent overly large step sizes that cannot be sufficiently reduced during high nonlinearity, a maximum allowable step size (Δt_{max}) is imposed. In the dynamic solver, the Δt_{max} is set equal to the sampling rate of the input loading signal (Ghezelbash, D'Altri, et al. 2025), which avoids significant artificial damping ($\Delta t_{max}/T < 10\%$ as explained in Section 5.2) and ensures that data is collected with the same fidelity as in benchmark experiments. Additionally, both solvers are configured with a minimum allowed step size (equal to $10^{-11}\times\Delta t_{max}$), a maximum number of iterations per step (10,000 times), and a maximum number of re-stepping attempts (15 times) in the event of non-convergence with the current step size. These parameters are calibrated to ensure that large nonlinearities are robustly handled without stability issues (through minimum step size and iteration limits), while also enabling the correct capture of physical instability in the simulated specimen (via the maximum re-stepping criterion), allowing the analyses to halt appropriately without generating purely numerical responses.

2.4. Dynamic energy dissipation

The dissipation of kinetic energy during dynamic simulations is governed by Rayleigh damping, introduced in the expanded blocks (Itasca 2020). The implicit-based HHT-α procedure enables the inclusion of both mass- and stiffness-proportional components of damping without negatively impacting simulation duration or computational demands as may occur with explicit-based solvers. The parameters governing Rayleigh damping (α_R for the mass-proportional term and β_R for the stiffness-proportional term) are calibrated based on the modal characteristics of the specimen under study and a target damping ratio (ζ_R). A value of $\zeta_R = 5\%$ is adopted in this study, consistent with previous works of the authors, where it has been shown to appropriately simulate the dynamic OOP response of one- and two-way spanning walls, as well as more geometrically complex gables (Ghezelbash, D'Altri, et al. 2025, 2026; Ghezelbash, Messali, and Rots 2023a). However, a limitation of the current damping methodology must be acknowledged. The damping parameters are calibrated at the beginning of the dynamic analyses and remain constant throughout the simulation. As a result, while the stiffness of the specimen may change due to the accumulation of damage, the Rayleigh damping continues to operate over the original frequency range to which it was calibrated. This may lead to over-damping of the damaged response, as previously noted in (Ghezelbash, Messali, and Rots 2023a). Nonetheless, this simplification is not expected to affect the outcomes of the present study for two main reasons. First, the study does not aim to capture the full progression of dynamic collapse; rather, it focuses solely on the onset of collapse. That is, the hysteretic response of specimens during collapse is not of interest here. Second, unlike prior applications of this modeling approach (Ghezelbash, D'Altri, et al. 2025, 2026; Ghezelbash, Messali, and Rots 2023a), the current study employs a simplified dynamic loading procedure involving simulations with a single run of dynamic motion. Since damage accumulation across multiple runs is not considered, the influence of the damping limitation is less severe. It should be noted that the aforementioned limitation is not unique to the use of Rayleigh damping and can also apply to other damping formulations.

3. Validation of the modeling approach: simulation of quasi-static settlement experiments

The modeling approach has already been extensively validated against dynamic OOP experiments of URM walls in (Ghezelbash, D'Altri, et al. 2025, 2026; Ghezelbash, Messali, and Rots 2023a), a repetition of similar validation is avoided here. Instead, the approach is validated in this section against settlement experiments to assess its suitability for the parametric analysis conducted in this study. The objective is to confirm that the approach can accurately reproduce the range of crack patterns and propagation paths expected under settlement loading. For this purpose, the experiments reported in (Bui et al. 2017; Gagliardo et al. 2021; F. Portioli and Cascini 2017) on URM walls and wallets subjected to base displacement are used as benchmarks, with the corresponding simulation results shown in Figure 2. These experiments, conducted on dry-joint specimens, are selected for three key reasons. First, experimental data on regular walls with mortar layers are scarce (Wang et al. 2021), and the available studies predominantly involve large façades or full buildings (Dalgic et al. 2023; Franza et al. 2022; Giardina et al. 2020), where accurate reproduction of boundary conditions introduces complexities that fall beyond the scope of this validation. Second, as dry-joint specimens, the simulation of the selected tests is more straightforward and less sensitive to material property uncertainties (Napolitano and Glisic 2019). Third, the specimens exhibit large crack openings and unit

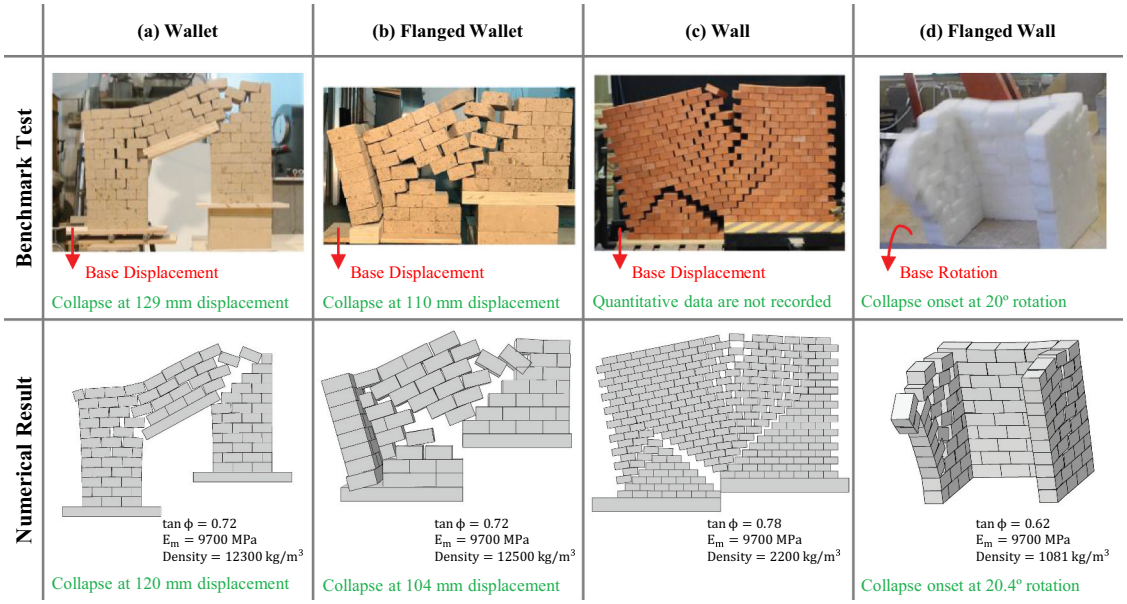

Figure 2. Validation of the modeling approach against settlement experiments on walls and wallets taken from (F. Portioli and Cascini 2017) (a) (Gagliardo et al. 2021), (b) (Bui et al. 2017), (c), and (Bui et al. 2017) (d). A small elastic slip of 0.001 mm and a large joint overclosure stiffness (k_{no}) of 221 N/mm^3 are considered in all simulations.

degradation; if these features are accurately captured in the simulations, they provide strong evidence of the ability of the modeling approach to track such responses without numerical instability.

In the simulations, the same boundary conditions, loading procedures, and geometrical configurations used in the original experiments are adopted. In addition, the unit density and the friction coefficient in the joints are taken directly from the reference publications (Bui et al. 2017; Gagliardo et al. 2021; F. Portioli and Cascini 2017), with the latter assigned to both bed and head joints. The remaining material input parameters are not calibrated, as cohesive response is neglected in the joints, and preliminary analyses have shown that the elasticity of the blocks does not influence crack propagation. Accordingly, the elastic modulus reported in (Bui et al. 2017) for the wall specimen (Figure 2(c)) is used for the blocks, as well as for the lintel (Figure 2(a)) and base components, across all simulations. The analyses are carried out under self-weight only (applied as gravity with $g = 9.81$ m/s^2), with base displacements or rotations applied and increased monotonically. The static solver introduced in Section 2.3 is employed for these simulations.

The deformation patterns and cracking of the numerical specimens are compared against the experimental benchmarks, along with loading magnitudes leading to or initiating collapse. The numerical simulations accurately replicate the experimental cracking and deformations across all specimens. Notably, the large block deformations and crack openings demonstrate the high stability of the modeling approach, even with the use of an implicit-based solver, achieved through the solver settings discussed in Section 2.3. Furthermore, the simulations capture complete detachment of blocks in both wall and wallet specimens, enabled by the use of contact-based joints. Finally, the numerically estimated deformation capacity of the specimens aligns very well with the experimentally recorded ones. In summary, these results confirm the capability of the numerical modeling approach to simulate settlement-induced damage, as well as to reproduce the correct crack progression in specimens with varying geometries.

4. Parametric analysis on OOP response of walls with settlement pre-damage

A visual summary of the parametric analysis conducted here to investigate the seismic OOP response of URM walls under settlement-induced pre-damage is presented in Figure 3. The study involves selecting various wall geometries, subjecting each to different settlement scenarios, and applying static or dynamic OOP loading at different pre-damage states. The subsequent sections describe each component of this procedure in more detail. Since the objective is to contribute to the assessment of the residential URM building stock in the Groningen province of Netherlands, which is currently exposed to induced seismic hazard (KNMI 2025), most

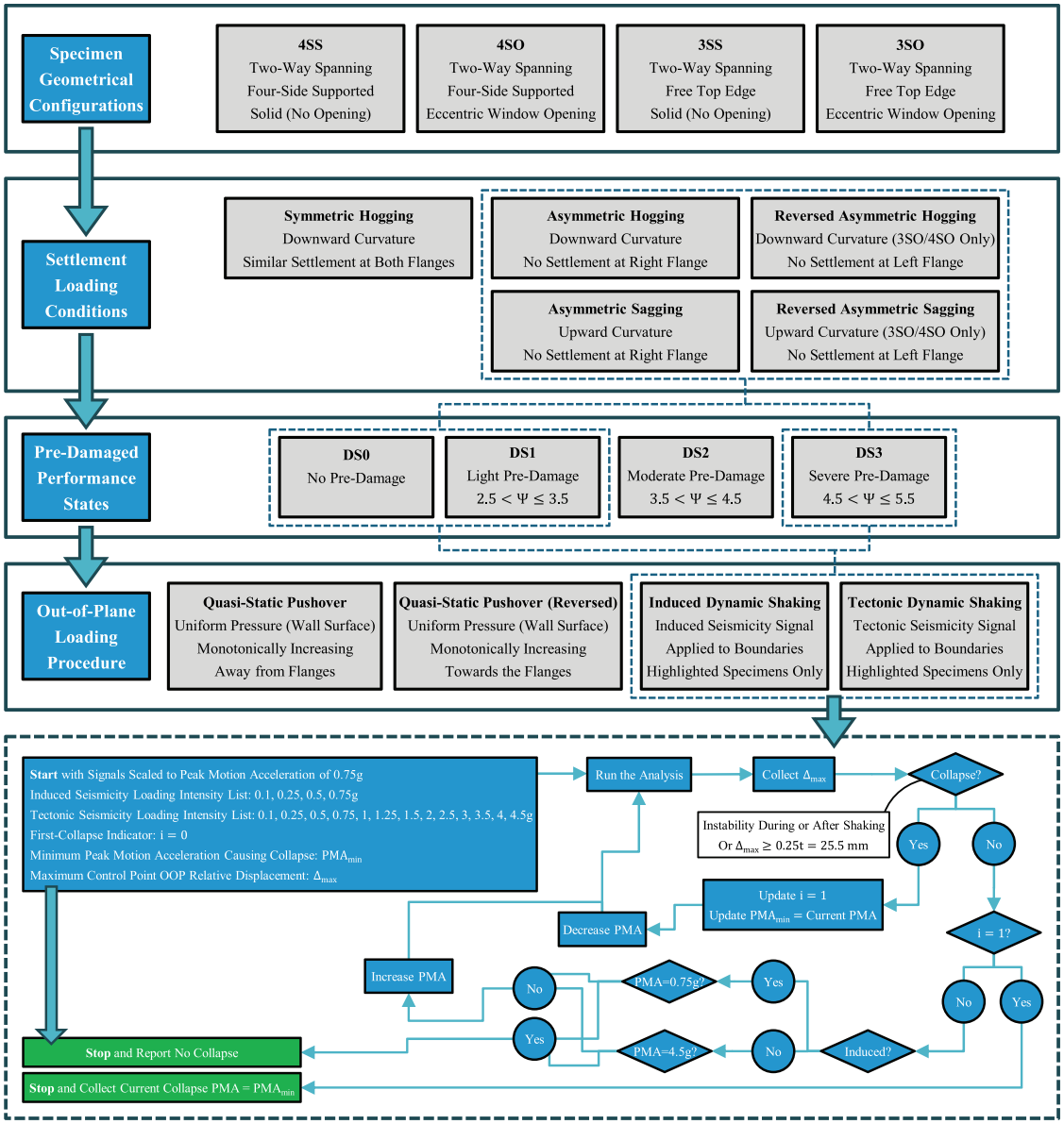

Figure 3. Overview of the parametric analysis procedure. In the pre-damaged performance states, Ψ is the damage parameter proposed in (Korswagen 2024).

of the decisions made at each stage of the study are informed by the geometrical, material, and loading characteristics typical of these buildings.

Based on the categorization proposed in (Ghezelbash, Rots, and Messali 2025), the interaction scenario investigated in this study (namely, the effects of settlement-induced pre-damage on the seismic OOP response) can be classified as a direct IP/OOP interaction scenario under sequential loading, or "SQ (IP, OOP)" for short. The following reasons support this categorization.

- Although settlement may cause both IP and OOP wall deformations, the majority of the deformations it triggers are IP. Hence, it is considered here an IP action.
- The interaction is driven by pre-damage, indicating a "sequential" (SQ) loading scenario. One might argue that, since the settlement-induced deformations are not removed prior to the application of OOP loading, the scenario could also fall under the combined (CB) category. However, the CB loading scenario refers to situations where pre-applied actions leave residual stresses that prevent a zero-stress state, whereas long-term settlement produces cracking that releases these stresses, so the structure is effectively stress-free at the onset of OOP loading.

- As the OOP response of the walls is directly influenced by their prior IP response, a "direct IP/OOP interaction" is indeed taking place.

4.1. Specimen geometries and mechanical properties

The four geometries shown in Figure 4 are used in the parametric analysis, representing walls typical of the residential URM building stock in the Groningen province of Netherlands (Tomassetti et al. 2019). All specimens are single-leaf, two-way-spanning walls, connected at their lateral edges to perpendicular elements, referred to as flanges, and at the bottom to a base that follows the planar geometry of the wall. They are assumed to be located on the ground floor of a building. This assumption is used because of the lack of an effective method for simulating settlement effects at upper levels (Prosperi et al. 2023, 2023a, 2023b). The assumption may limit the applicability of the outcomes of this study, since upper-floor walls are typically more vulnerable to OOP loading (Tomassetti et al. 2019) and thus require greater attention. However, it is deemed acceptable here since the current study is the first attempt to study seismic behavior of walls under settlement-induced pre-damage. Future research is required to investigate the OOP response of full façades or methodologies for applying pre-damage to upper-floor walls.

For brevity, each specimen is referred to using an 'iSX' naming convention, where 'i' indicates the number of supported edges (i.e., 4 or 3), and 'X' indicates the presence of openings ('O' for opening walls, 'S' for solid walls). Two specimens, referred to as 4SS and 4SO, are connected at the top to a beam simulating the diaphragm of an upper floor in a two-story building. The other two specimens, 3SS and 3SO, have a free top edge, representing walls that do not support upper floors. Among these, 4SS and 3SS are solid walls (no openings), while 4SO and 3SO feature an eccentric window opening with a top lintel. The specimens are constructed using the numerical modeling approach adopted in this study, outlined in Section 2, with expanded blocks measuring $222 \times 81 \times 102\ \text{mm}^3$ (length × height × thickness) in a running bond configuration. The main wall dimensions are $3978 \times 2754 \times 102\ \text{mm}^3$, with 1096 mm-long flanges matching the height and thickness of the wall. In specimens 3SO and 4SO, the window measures $1776 \times 1620\ \text{mm}^2$ (length × height), covering 26% of the main wall surface. The large pier in these specimens is 1545 mm long, and the spandrel beneath the opening is 567 mm high. The lintel spans the top of the opening, is two blocks high, and extends half a block length beyond each side of the opening. The geometry and opening configuration of these specimens are based on the walls tested under shake table loading in (Graziotti et al. 2019) and simulated by the authors in (Ghezelbash, Sharma, et al. 2025).

The mechanical behavior of the expanded blocks and zero-thickness joints, represented by the parameters shown in Figure 1, is defined using the input values listed in Table 1. These parameters are calibrated against material-level experiments (Messali et al. 2020) conducted on URM units and assemblies used in Dutch residential construction in the Groningen region (Jafari, Esposito, and Rots 2019), specifically Calcium Silicate solid bricks and general-purpose cement-based mortar. The calibration procedure involves simulating the material experiments to extract the required input parameters (D'Altri et al. 2019). Wallet compression and unit three-point bending tests are used to calibrate the elastic, compressive, and tensile responses of the expanded blocks. The former is also used to calibrate the overclosure stiffness of the joints. Triplet shear and wallet four-point bending tests (parallel to the bed joints) are employed to calibrate the shear and tensile responses of the joints. The density and Poisson's ratio (ν_m) of the blocks are taken as the average of

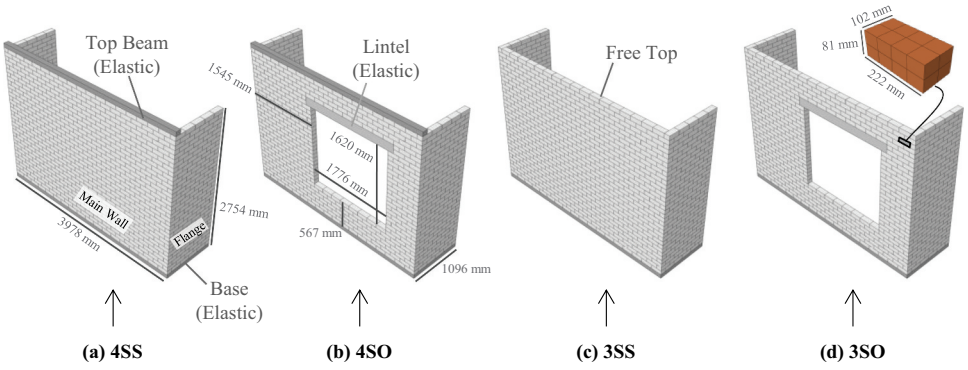

Figure 4. Geometry of the specimens modelled in the parametric analysis.

Table 1. Mechanical characterization input parameters for the parametric analysis.

Expanded Blocks							
Elastic Behavior		CDP Parameters		Compressive Behavior		Tensile Behavior	
E_m[MPa]	4800	ψ[°]	10	$f_m^{'}$[MPa]	6.35	f_{bt}[MPa]	1.83
ν_m[−]	0.16	[−]	0.1	ε_{mp}[−]	0.004	ε_{btk}[−]	0.004
Density[kg/m^3]	1708	f_{b0}/f_{c0}[−]	1.16	ε_{mk}[−]	0.016		
		ρ[−]	2/3				
Zero-Thickness Joints							
Overclosure Behavior		Tensile Cohesive Behavior		Shear Cohesive Behavior		Shear Frictional Behavior	
k_{no}[N/mm^3]	221	k_{nt}[N/mm^3]	221	k_s[N/mm^3]	87	tanϕ[−]	0.57
		f_t[MPa]	0.096	c[MPa]	0.11	δ_e[mm]	0.001
		u_k[mm]	0.3	δ_k[mm]	0.3		

experimentally recorded values (Jafari and Esposito 2016; Messali et al. 2020). Finally, the Concrete Damaged Plasticity (CDP) model parameters follow typical values used for quasi-brittle materials such as URM (Lubliner et al. 1989; Milani, Valente, and Alessandri 2018; Scacco et al. 2020), with an eccentricity (ε) of 0.1, a biaxial-to-uniaxial initial compressive strength ratio (f_{b0}/f_{c0}) of 1.16, and a tensile-to-compressive meridian ratio (ρ) of 2/3. The dilatancy angle (ψ) is set to 10°, based on prior experimental and numerical studies (Castellazzi et al. 2017; Mirmiran and Shahawy 1997). This calibration approach has been shown in (D'Altri et al. 2019; Ghezelbash, Sharma, et al. 2025) to result in accurate simulations of wall- and building-level response without requiring further micro-adjustment of the input parameters. Therefore, further demonstration of the validity of the modeling approach for simulating wall-level OOP responses, previously shown in (D'Altri et al. 2019; Ghezelbash, D'Altri, et al. 2025; Ghezelbash, Messali, and Rots 2023b; Ghezelbash, Sharma, et al. 2025), is omitted here for brevity. It should be noted that the lintel (4SO/3SO), the base (all specimens), and the top beam (4SS/4SO) are modeled as elastic elements with the same material properties as the expanded blocks. Their finite element discretization follows the same mesh resolution as the expanded blocks to ensure conformity at the contact interfaces. The head and bed joints are assigned identical material properties, assuming uniform construction quality. Similarly, the joints connecting the lintel, base, and top beam to the blocks are assigned the same properties as the head and bed joints for simplicity, following previous studies of the authors (D'Altri et al. 2019; Ghezelbash, D'Altri, et al. 2025). Finally, modal analysis is performed on each pristine specimen to identify the natural frequencies of their deformation modes for Rayleigh damping calibration.

4.2. Settlement loading procedure

The boundary conditions used for the application of settlement are illustrated in Figure 5(a). The main walls are positioned in the x-y plane, with the flanges extending in the positive z-direction. The boundary condition idealization procedure with reference points, previously used in the simulation of two-way spanning walls in (Ghezelbash, Sharma, et al. 2025), is adopted here. It allows straightforward switching between settlement and OOP loading conditions, the latter shown in Figure 5(b). Accordingly, at the top of each flange, excluding the block at the wall-flange intersection, a kinematic coupling is established between the flange surface and a reference point located at its geometric center. The coupling assumes the surfaces to behave as a rigid region that deforms according to the degrees of freedom (DoFs) of its corresponding reference point. A similar kinematic coupling is applied at the back of each flange, extending from the bottom up to three block rows below its top. In the 4SS and 4SO specimens, the top beam is also kinematically coupled to a reference point located at its mid-thickness, mid-length position, and aligned with the top edge of the topmost block row. To enable settlement application, the bottom boundary conditions are applied directly to the base, without the use of a reference point. It should be noted that, while the couplings considered at the top of the main walls and flanges are not expected to compromise the representation of realistic boundary conditions, as they mimic walls connected to rigid diaphragms, the couplings at the back ends of the flanges may introduce over-constraint. Specifically, in real buildings, perpendicular walls are longer than the flanges considered in this study, which allows them to develop cracks and exhibit OOP deformation during the IP deformation of the main wall, such as under settlement. Nevertheless, the current setup is maintained to simplify the application of boundary

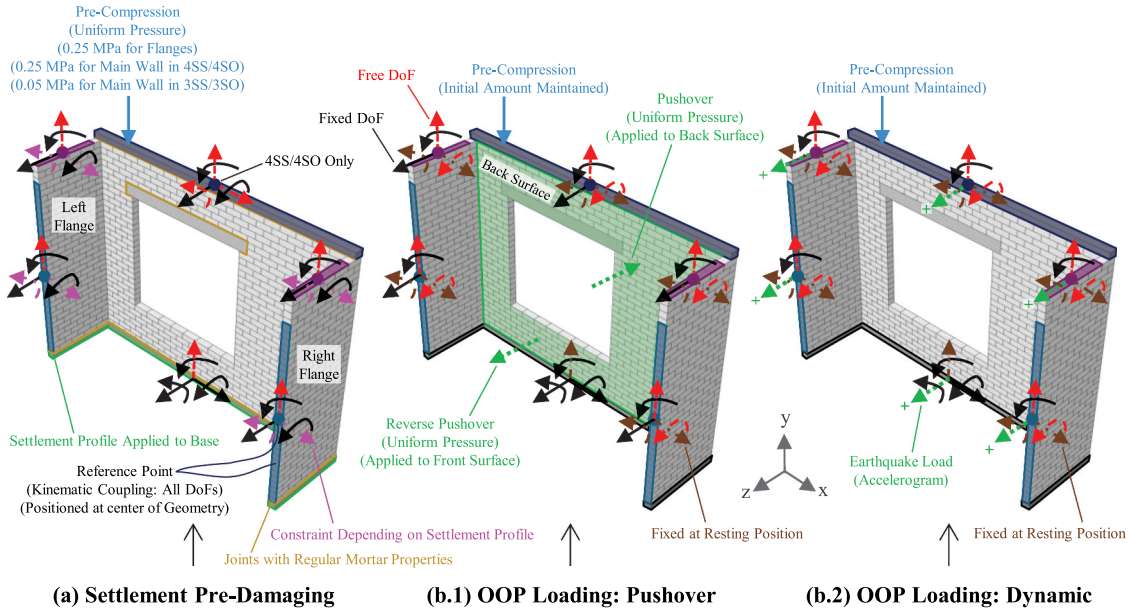

Figure 5. Boundary conditions used for settlement and OOP loading in the parametric analysis. The 4SO wall is shown as it represents the most complex geometry used in this study.

conditions, keep the simulations consistent with the experiments the modeling approach is calibrated against, and to represent an extreme scenario of the structural responses, as further explained at the end of this section.

Prior to the application of settlement, gravity, and vertical overburden loads are applied using the static solution procedure. The vertical overburden is applied to the top of the flanges and the main wall. For the 4SS and 4SO specimens, an overburden of 0.25 MPa is applied to the top of both flanges and the top of the top beam, representing the typical load from a bi-directional floor diaphragm in a two-story URM building in Netherlands (Messali et al. 2020). For the 3SS and 3SO specimens, the same 0.25 MPa value is applied to the flanges, but a lower overburden (0.05 MPa) is applied to the main wall, consistent with conditions where unidirectional floor diaphragms are supported only by the flanges (Messali et al. 2020). To simulate the weight of structural components (e.g., walls) resting above the panels (Graziotti et al. 2019), the pre-compression in the 3SS and 3SO walls is not reduced to zero. During the application of vertical loading, the base is fully fixed, while all reference points are free to displace in all their DoFs. In the 4SS and 4SO specimens, the main wall pre-compression is applied at the top of the top beam, whereas in the 3SS and 3SO specimens, it is applied directly to the top of the main wall. It should be noted that the pre-compression remains constant throughout the subsequent settlement and OOP loading phases. As a consequence, the parametric analysis does not explore the influence of pre-compression on settlement-induced damage effects.

Settlement loading is applied using the static solution procedure. The displacements are imposed on the base parts, rather than directly on the bottom row of blocks, to avoid overexciting the walls and to allow them to respond naturally to the imposed settlement. Soil–structure interaction is not explicitly modeled (Longo et al. 2021), and the applied settlement at the base is conservatively assumed to be equal to the vertical displacement recorded in the underlying soil, deliberately neglecting the horizontal displacements, which may be more relevant for cases of tunnelling, mining, or excavation works rather than natural subsidence (Boscardin and Cording 1989; Prosperi, Korswagen, et al. 2025). The five settlement profiles used in this study are shown in Figure 5. These are two-dimensional vertical displacement profiles applied along the y-axis (vertical direction), with varying magnitudes along the x-axis (the length of the wall). The portions of the base beneath the flanges are displaced in accordance with the corresponding ends of the main wall panel, neglecting any variation of settlement along the z-axis (flange direction). This neglect of settlement variations in the z-direction (studied in (Zhao and DeJong 2023)) is justified by the relatively short lengths of the flanges.

The settlement profiles used in the study include one symmetric hogging profile (Figure 6(a)), two asymmetric hogging and sagging (Figure 6(b)) profiles, and two reversed variations of the asymmetric profiles (Figure 6(c)). The symmetric hogging profile causes

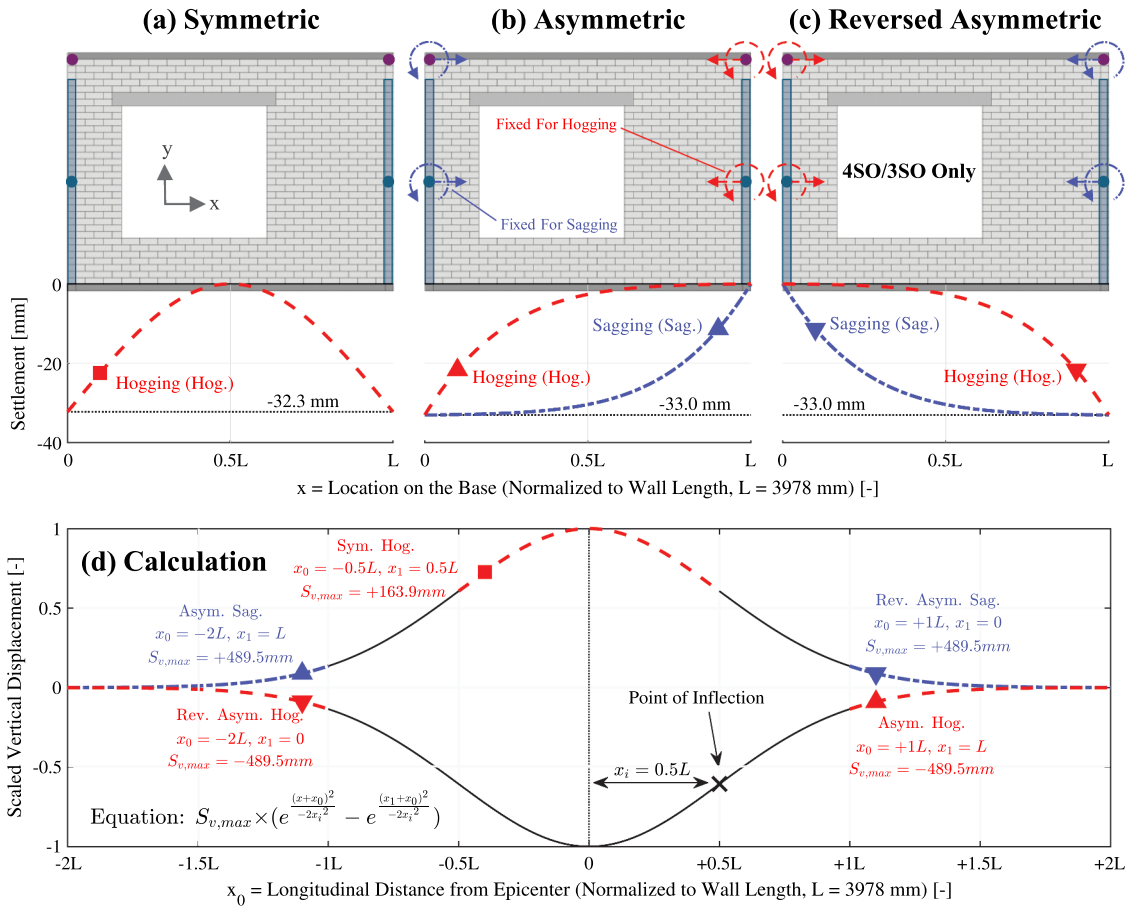

Figure 6. Vertical displacement profiles applied at the base of the walls for settlement loading: symmetric (a), asymmetric (b), and reversed asymmetric (c) displacement profiles scaled to angular distortion of 50‰, and their calculation from the Gaussian bell curve (d).

equal vertical base deformation at both ends of the walls, whereas the asymmetric profiles produce vertical base deformation at only one wall end, while the other end remains at zero settlement. The reversed asymmetric profiles, in which the wall end kept at zero settlement is opposite to that in the regular asymmetric profiles, are applied only to the 4SO and 3SO specimens to investigate the influence of opening eccentricity on the wall response to settlement. These profiles are generated following the methodology proposed by (Peck 1969), using the Gaussian normal distribution curve, as also adopted in (Korswagen et al. 2024; Prosperi, Longo, et al. 2025) and illustrated in Figure 6d. Although originally developed to simulate ground deformations due to tunneling, this approach has been shown to be applicable to other forms of subsidence, such as gas extraction, which is particularly relevant to the Groningen province in Netherlands (KNMI 2025; Prosperi 2025). The settlement is applied monotonically, increasing up to a maximum angular distortion, defined in (Burland and Wroth 1975), of $\beta = 50‰$ (1/20 rad), until collapse occurs. The final value of β ensures that the applied settlement is sufficiently large to activate all possible crack paths within the specimens. Collapse during settlement is identified as the inability of the specimen to maintain static equilibrium, i.e., through the falling of blocks or larger sections.

During symmetric settlement, the flange reference points are free to translate in the x-direction, uplift (in y-direction), and rotate about the z-axis. In contrast, during asymmetric settlement, all DoFs at the top and back reference points of the flange located at the zero-rotation end of the profile are constrained, except for vertical uplift. For example, in the asymmetric hogging and sagging cases (Figure 5b), the right and left flanges, respectively, are constrained. This setup does not fully conform to the actual boundary conditions of walls in real buildings, in which both ends of the walls can deform freely under settlement. Although a more realistic configuration would have involved increasing the flange length to allow greater flexibility at the wall ends and damage propagation into the flanges, this option was not pursued for two reasons. First, it would have required modifying the wall geometries for which

the modeling approach had already been calibrated, thereby necessitating additional calibration steps. Second, the current setup is intentionally adopted to suppress rigid-body motion and enforce cracking at the wall-flange connections, thus representing an extreme damage scenario. Third, the inclusion of flanges in this study is intended to avoid the need to impose two-way bending OOP boundary conditions through the direct restraint of the wall side edges, rather than to replicate flange–wall interactions. Future studies should pursue more methodological approaches for the selection of flange geometries and constraints.

4.3. Pre-damage states: initial conditions for OOP loading

Several performance states, referred to here as pre-damage states, are identified for each specimen and used as initial conditions for subsequent OOP loading. These pre-damage states are defined based on the EMS-98 criteria (Grünthal 1998), as summarized in Table 2. They are labeled as "DSi," where "i" ranges from 0 to 4, with DS0 indicating pristine conditions and higher values representing increasing levels of pre-damage. The pre-damage states are identified using both qualitative and quantitative indicators. DS1 (light pre-damage) corresponds to the appearance of the first visible cracks, with representative crack widths (C_w) up to 5 mm. DS2 (moderate pre-damage) is associated with more widespread cracking, with widths reaching up to 15 mm. DS3 (severe pre-damage) is defined by the formation of a complete crack pattern across the specimen, with crack widths up to 25 mm. DS4 (very severe pre-damage or near-collapse) involves significant structural deformation and wider cracks. In this study, DS4 is excluded from the subsequent OOP analyses to maintain the practicality of the investigation: buildings reaching DS4 are typically considered unsafe and require repair, reconstruction, or demolition (Boscardin and Cording 1989; Burland, Broms, and De Mello 1977; Giardina 2013).

While each damage state is traditionally identified using the crack-based criteria described above, this study adopts the scalar damage parameter (Ψ) proposed in (Korswagen 2024). In real-world structures, severe damage may occur through the formation of numerous long but narrow cracks, or conversely, through fewer cracks with large widths but limited lengths. These conditions can, respectively, lead to an underestimation or an overestimation of damage severity when relying solely on traditional, width-based criteria (Z. Q. Chen and Hutchinson 2010). The Ψ parameter offers a more objective alternative by accounting not only for crack widths, but also for their lengths and frequency, thereby providing a more realistic assessment of damage severity (Korswagen 2024). Equation 1 is used to calculate Ψ based on the number of cracks (n), their lengths ($C_{L,i}$ in mm), and widths ($C_{w,i}$ in mm). The $C_{w,i}$ combines both shear and normal components of the crack. Each crack is assigned a numerical "i" identifier.

$$\Psi = 2n^{0.15}\left(\frac{\sum_{i=1}^{n} C_{L,i}C_{w,i}^{2}}{\sum_{i=1}^{n} C_{L,i}C_{w,i}}\right)^{0.3} \quad (1)$$

The ranges of Ψ recommended in (Prosperi 2025) and listed in Table 2 are used to identify the different pre-damage states. During settlement application, the evolution of cracks is monitored at every 0.625‰ (1/1600) increment of angular distortion. The point in the loading history at which the calculated Ψ value falls within the expected range of a given pre-damage state is selected and used as the initial condition for the corresponding OOP analysis. Modal analysis is also performed on the specimens at different pre-damage states prior to the application of OOP loading, to identify the effects of settlement on the fundamental frequencies and natural deformation modes.

Table 2. Criteria adopted for the identification of settlement-induced damage states.

Classification				C_w (Boscardin and Cording 1989; Burland, Broms, and De Mello 1977)	Ψ (Prosperi 2025)
State	Damage Class	Description	Repair (Grünthal 1998)		
DS0	No Damage	–	–	–	–
DS1	Light[a]	First Visible Cracks	Easy	1–5 mm	2.5–3.5
DS2	Moderate	Many Visible Cracks	Medium	5–15 mm	3.5–4.5
DS3	Severe[b]	Full Crack Patterns	Extensive	15–25 mm	4.5–5.5
DS4	Near Collapse[c]	Large Deformations	Rebuild	>25 mm	>5.5

[a]Also known as Slight or Negligible.
[b]Also known as Heavy.
[c]Also known as Very Severe or Very Heavy. This state is not considered in the current study.

4.4. OOP analysis procedure

After settlement, a relaxation period is introduced via a static analysis step. The specimens are then subjected to different types of OOP analyses, two static pushover and two dynamic shaking scenarios, as illustrated in Figure 5b1,b2, respectively. The static analyses are conducted as simplified simulations, commonly used in high-fidelity modeling in both research and practice (Patel and Dubey 2022, 2023; Sharma et al. 2021), primarily due to the high computational demands of unit-by-unit dynamic simulations. The goal of the static analyses in this study is to assess their ability to capture the effects of settlement-induced pre-damage and to evaluate whether they can serve as practical alternatives to dynamic analyses. The static simulations (relaxation and pushover) are performed using the static solver introduced in Section 2.3. They involve the application of a uniformly distributed pressure to the surface of the main wall, which is monotonically increased until collapse (defined by large deformations and physical detachment of portions of the wall) is reached. In one set of analyses, the pressure is applied to the back surface of the main wall, pushing it in the negative z-direction, away from the flanges. In the second set, referred to as "reversed pushover" hereafter, pressure is applied to the front surface, pushing in the positive z-direction, toward the flanges. Due to the geometric asymmetry of the specimens with respect to the OOP loading direction (with flanges located only on one side), both loading directions are necessary to investigate the pre-damage effects on lower- and upper-bound OOP strengths, respectively.

During the pushover simulations, the base of each wall is fully fixed at its final position corresponding to the specific pre-damage state (Figure 5b1). The reference points of the flanges and the top beam are also fixed at their final positions but vertical uplift and rotation about the x-axis are permitted. These boundary conditions closely replicate those used in dynamic experiments and follow the setup adopted in (Graziotti et al. 2019) and the corresponding numerical simulations by the authors in (Ghezelbash, Messali, and Rots 2023a). The free rotation of the top beam in the 4SS and 4SO specimens conservatively simulates the response of flexible floor diaphragms, since more constrained diaphragm configurations are expected to yield higher OOP strengths (Ghezelbash, Sharma, et al. 2025). Finally, pressure is always applied perpendicularly to the wall surface. As a result, when walls undergo large OOP deformation, the direction of the pressure dynamically adjusts to remain perpendicular, a simplifying assumption intended to streamline the analysis, while disregarding the fixed-direction nature of seismic loads.

Two sets of dynamic analyses are performed using the HHT-α solver introduced in Section 2.3, each employing a different loading signal, as shown in Figure 7. The first set uses a signal representing the induced seismicity hazard in the Groningen province

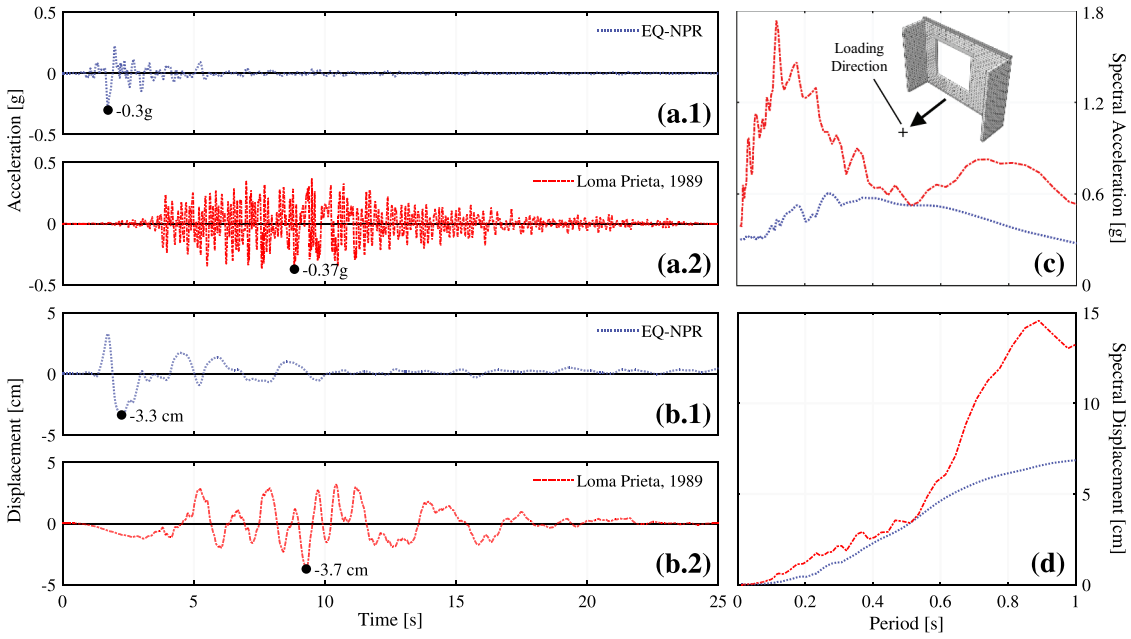

Figure 7. Dynamic motions used for the dynamic simulations of the parametric analysis: acceleration time histories (a), their resultant displacements (b), and 5%-damped acceleration (c) and displacement spectra (d) of the induced-seismicity (Miglietta et al. 2021) (1) and tectonic-seismicity (Ancheta et al. 2014) (2) signals.

of Netherlands. This signal, referred to as EQ-NPR, is adapted from the shake table test of a full-scale building reported in (Miglietta et al. 2021). The second set uses a tectonic seismicity signal extracted from the NGA-West2 database (record number 811) (Ancheta et al. 2014), recorded during the 1989 Loma Prieta earthquake in Central California, USA (2019). Both signals are characterized by high peak motion accelerations (PMAs) of approximately 0.3 g. However, the tectonic signal contains multiple acceleration peaks (Figure 7a2) and exhibits a longer significant duration (Figure 7b2). In addition, it demonstrates much larger spectral accelerations (Figure 7c). Given the force-controlled nature of the two-way OOP response simulated in this study, such differences are expected to influence the dynamic response of the specimens. In fact, the selection of signals with differing seismic hazard sources is intended to explore these effects. The accelerograms are used in their raw form, having already been post-processed in the original references. The signals are applied in the positive z-direction to the entire base of the specimens, as well as to the reference points of the flanges and top beam (Figure 5b2). The other DoFs at the base are fully fixed at their final positions reached at the end of the settlement phase. Similarly, the flange and top beam reference points are only allowed vertical uplift and rotation about the x-axis. The direction of dynamic loading is specifically selected to align the direction of PMA in both signals with the weak OOP direction of the specimens (away from the flanges). Based on the sampling interval of the loading signals, a $\Delta t_{max} = 0.0025$ s is used for both induced and tectonic dynamic analyses.

Dynamic simulations are conducted using an Incremental Dynamic Analysis (IDA) approach, following the procedure illustrated in Figure 3. For each specimen, starting from a pre-damage state caused by a given settlement profile, the dynamic analysis begins with the loading signal scaled to a PMA of 0.75 g. Based on the simulation outcome, the subsequent steps proceed as follows:

- If the specimen collapses, a new analysis is performed on the pristine specimen using a lower PMA. This process is repeated until a simulation is found in which the specimen does not collapse. In this case, the lowest loading intensity that leads to collapse is identified as the collapse PMA of the specimen.
- If the specimen does not collapse, the PMA is increased, and the simulation is repeated on the specimen, restarting from the conditions corresponding to the considered damage state. The process is repeated until collapse occurs. The lowest intensity at which collapse first occurs is then taken as the collapse PMA of the specimen.

The increase or reduction in loading intensity follows a predefined list of PMAs, as shown in Figure 3. For simulations using the induced seismicity signal, this list is limited to a maximum PMA of 0.75 g to maintain practical relevance: in real-world scenarios, induced earthquakes are typically low in amplitude and rarely exceed intensities of 0.5 g (Bommer et al. 2022; Edwards et al. 2019). As such, scaling the induced loading signal beyond 0.75 g is considered to yield results of limited meaning. Therefore, if a specimen does not collapse under the induced signal at 0.75 g, the IDA for that case is terminated, and no-collapse outcome is declared.

In IDAs, collapse is typically defined as the inability of the specimen to maintain equilibrium during dynamic loading (Ghezelbash, Sharma, et al. 2025), corresponding to the falling of portions of the wall or complete wall failure. However, an additional deformation-based criterion is adopted in this study to provide a more practical and engineering-relevant definition of collapse. Specifically, collapse is assumed to occur as soon as OOP deformations equal to or exceeding 25% of the wall thickness ($t = 102$ mm) are observed during dynamic loading. This displacement-based criterion aligns with real-world engineering practice, where walls exhibiting such large OOP deformations are typically considered severely damaged and are deemed unusable without repair or the installation of temporary countermeasures (FEMA 306: Evaluation of Earthquake Damaged Concrete and Masonry Wall Buildings 2000; Burton and Deierlein 2018; Di Ludovico et al. 2021; Taucer and Pinto Vieira 2007). The 25% threshold is based on prior dynamic OOP simulations of one- and two-way spanning walls and gables (Ghezelbash, D'Altri, et al. 2025, 2026; Ghezelbash, Sharma, et al. 2025), as well as more complex sub-structures (Ghezelbash, Aşıkoğlu, et al. 2025). In the latter, the same criterion was used to predict collapse under 29 different earthquake records in a blind prediction contest, yielding accurate predictions and correctly identifying the number of collapsed specimens. The use of this criterion also addresses limitations in the numerical modeling procedure. As shown in (Ghezelbash, Sharma, et al. 2025), in cases involving specimens similar to the 3SS and 3SO walls in this study, collapse may not occur numerically even after the formation of complete crack patterns. Instead, disconnected portions may undergo very large, physically unrealistic deformations, due to overdamping effects or the absence of element deletion in the simulations. The 25% deformation threshold prevents such cases from being misinterpreted as non-collapse.

The dynamic analyses discussed above are conducted only for specimens in DS0, DS1, and DS3 pre-damage states. Additionally, specimens pre-damaged under

symmetric hogging are excluded from the dynamic analyses, as the settlement profile used is considered too extreme and not representative of realistic ground movements (see Section 4.2). Furthermore, the type of damage induced by symmetric hogging is similar to that caused by asymmetric profiles. In all dynamic analyses, the motion is applied uniformly to all specimen boundaries, neglecting building-level amplification effects. This simplification is acceptable because the walls are assumed to be on the ground floor, where such amplification is minimal, and ground-shaking records are appropriate.

5. Results and discussion

This section presents the results obtained from each step of the parametric analysis. Section 5.1 outlines the range of structural responses under settlement loading, highlighting differences in damage evolution across specimens and loading scenarios. Section 5.2 discusses the outcomes of modal analyses performed on both pristine and pre-damaged specimens, with the latter interpreted in terms of changes to OOP stiffness. Section 5.3 presents the results of static pushover OOP analyses, comparing peak strength and failure mechanisms between pre-damaged and pristine specimens. Finally, Section 5.4 describes the dynamic OOP analysis outcomes and examines how specimen response differs under dynamic loading compared to that observed in the static analyses.

5.1. Settlement loading: damage patterns and pre-damage states

The damage patterns obtained at the end of the application of the considered settlement scenarios are presented in Figure 8. Walls subjected to hogging exhibit various cracking patterns, including vertical and diagonal cracks in the main panels (4SS/3SS) and large piers (4SO/3SO), diagonal cracks at the corners of openings (4SO/3SO), and detachment of the flanges from the base. In contrast, walls subjected to sagging show more localized damage, primarily concentrated at the bottom mortar joints and the panel-flange connections. In the 4SO and 3SO specimens, sagging-induced damage also includes the extension of a base crack along a diagonal stepping path toward the bottom of the opening, as well as cracking at the corners of the lintel that propagates to the top of the main wall. These responses result from the lower horizontal and vertical confinement in the walls due to the presence of the window. Overall, small sensitivity of damage to the symmetry of the settlement profile is observed. An exception is given by the 4SS specimen, which exhibits a single dominant crack under asymmetric hogging, compared to two cracks under the symmetric profile. The key distinction between symmetric and asymmetric settlement cases lies in the angular distortion required to reach the final cracked state: the asymmetric cases require significantly larger distortions, in some cases up to twice as large (see Section 4.3). With respect to the direction of asymmetric settlement profiles in the 4SO and 3SO specimens, a notable difference in damage response is observed. Reversed asymmetric profiles cause more severe crack propagation, which is attributed to the mobilization of the larger pier.

Figure 9 illustrates examples of how different settlement-induced pre-damage states are identified in specimens under symmetric hogging. For consistency, cracks at a given location within a specimen are assigned the same identifier across all pre-damage states. In the calculations, all cracks, including those within the main wall, flanges, and base mortar joint, are included. Three conservative and simplifying assumptions are adopted in the analysis. First, cracks with the same origin and propagating in multiple directions (e.g., those beneath the window in the 4SO/3SO specimens) are treated as a single crack. Second, cracks that change direction (e.g., those observed in the 4SS/3SS walls or originating from the top corner of the long pier in the 4SO wall) are considered continuous. Third, for each crack, the maximum width observed along its length is taken as its representative width. The difference between the use of the Ψ parameter and the use of traditional damage-state detection methods (based on a single crack width) is particularly evident in the 4SS and 4SO specimens. In these cases, DS3 occurs at maximum crack widths of 12.8 mm and 12.3 mm, respectively, values about 35% below the median of the typical range used in conventional criteria (20 mm shown in Table 2). However, the overall state of these specimens, including the formation of complete crack patterns, clearly aligns with the qualitative definition of DS3.

The angular distortions at which light (DS1) to severe (DS3) damage occurs in different specimens and settlement scenarios are listed in Table 3. Based on the data, and consistent with the findings of previous studies (Prosperi, Longo, et al. 2025), symmetric hogging is identified as the settlement profile that causes the most rapid damage evolution, reaching each pre-damage state at a lower angular distortion value across all specimens considered. However, it should be noted that this accelerated damage may be attributed to the extreme settlement conditions adopted in the current study. Specifically, the point of inflection in the Gaussian bell curve used to define the settlement profiles is assumed to occur at a distance equal to half the wall length (L/2 in

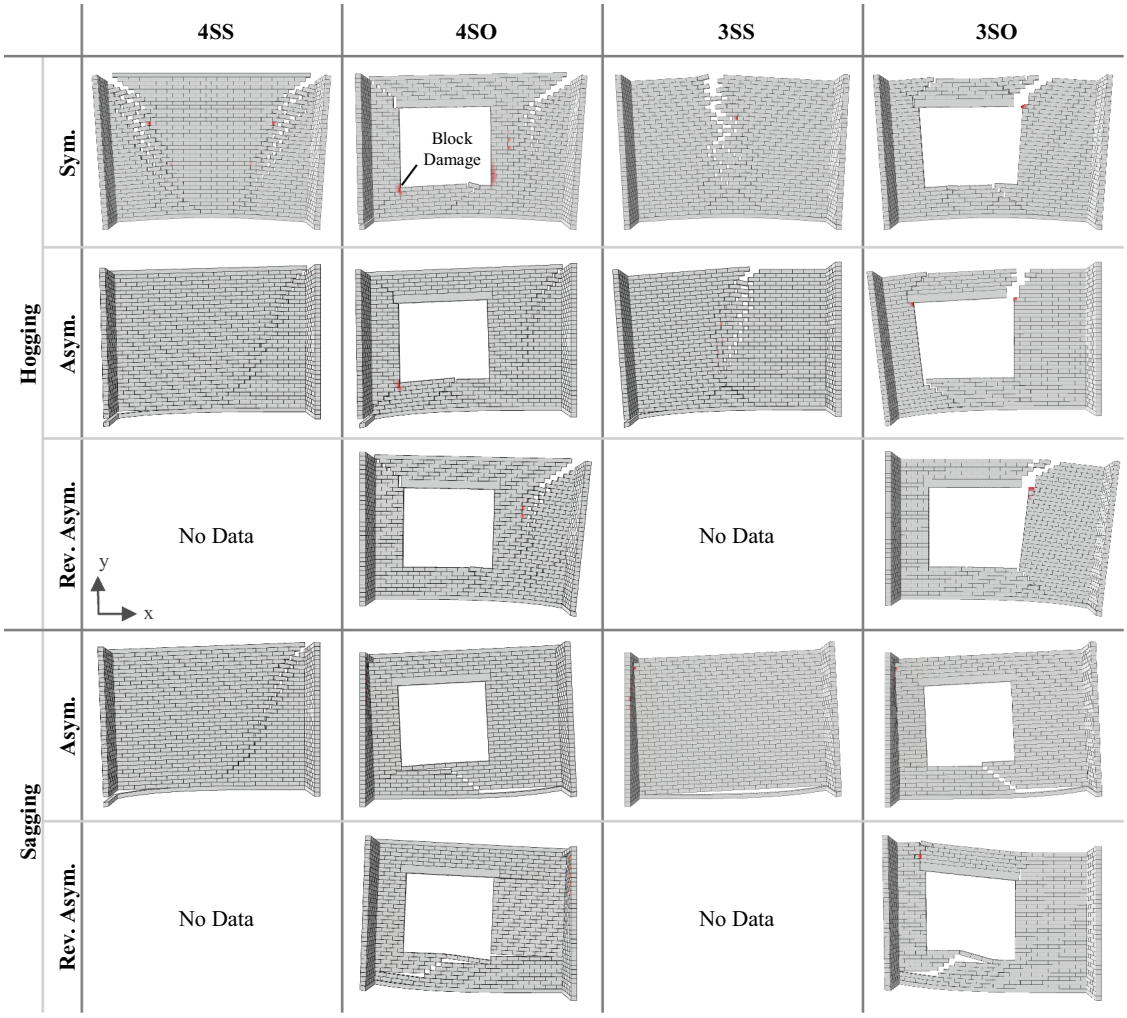

Figure 8. Final crack patterns after the application of settlement loading. Damage in the blocks (i.e., crushing or tensile cracking) is highlighted in red. The deformed shapes are magnified with various scales for clear visualization of the crack paths.

Figure 6d). In real-world conditions, this point is typically located much farther away, producing lower-curvature profiles (Prosperi 2025). As a result, higher angular distortions are needed to achieve similar damage states, compared to the simulations presented here. Asymmetric hogging and sagging settlement profiles reach DS3 at angular distortion values ranging from 8.1‰ to 18.1‰, significantly higher than the real-world limit values reported in the literature, which are typically up to 3.3‰ (1/300) (Giardina 2013; Korswagen 2024). This suggests that if buildings are rehabilitated upon reaching such practical distortion thresholds, these types of settlement profiles may not lead to severe damage.

The specimens exhibit varying sensitivities to the type of asymmetric settlement, depending on their geometry. While the 4SS and 3SS specimens show faster damage progression under asymmetric hogging, the 4SO and 3SO specimens exhibit similar angular distortion thresholds for reaching different pre-damage states under both asymmetric sagging and hogging. In the solid walls, benefiting from higher horizontal confinement, sagging damage is primarily concentrated at the base mortar joint. This damage mechanism requires relatively high angular distortions to initiate. In contrast, in walls with openings, the lower horizontal confinement leads to more distributed damage under sagging. Cracks initiate at the base joint and propagate toward the window, with additional cracks observed around the lintel. As a result, walls with opening reach higher pre-damage states at lower angular distortions due to increased crack development. With respect to the direction of the asymmetric settlement profile, both specimens with opening show faster damage progression under reversed asymmetric settlement, attributed to the increased mobility and cracking of their larger

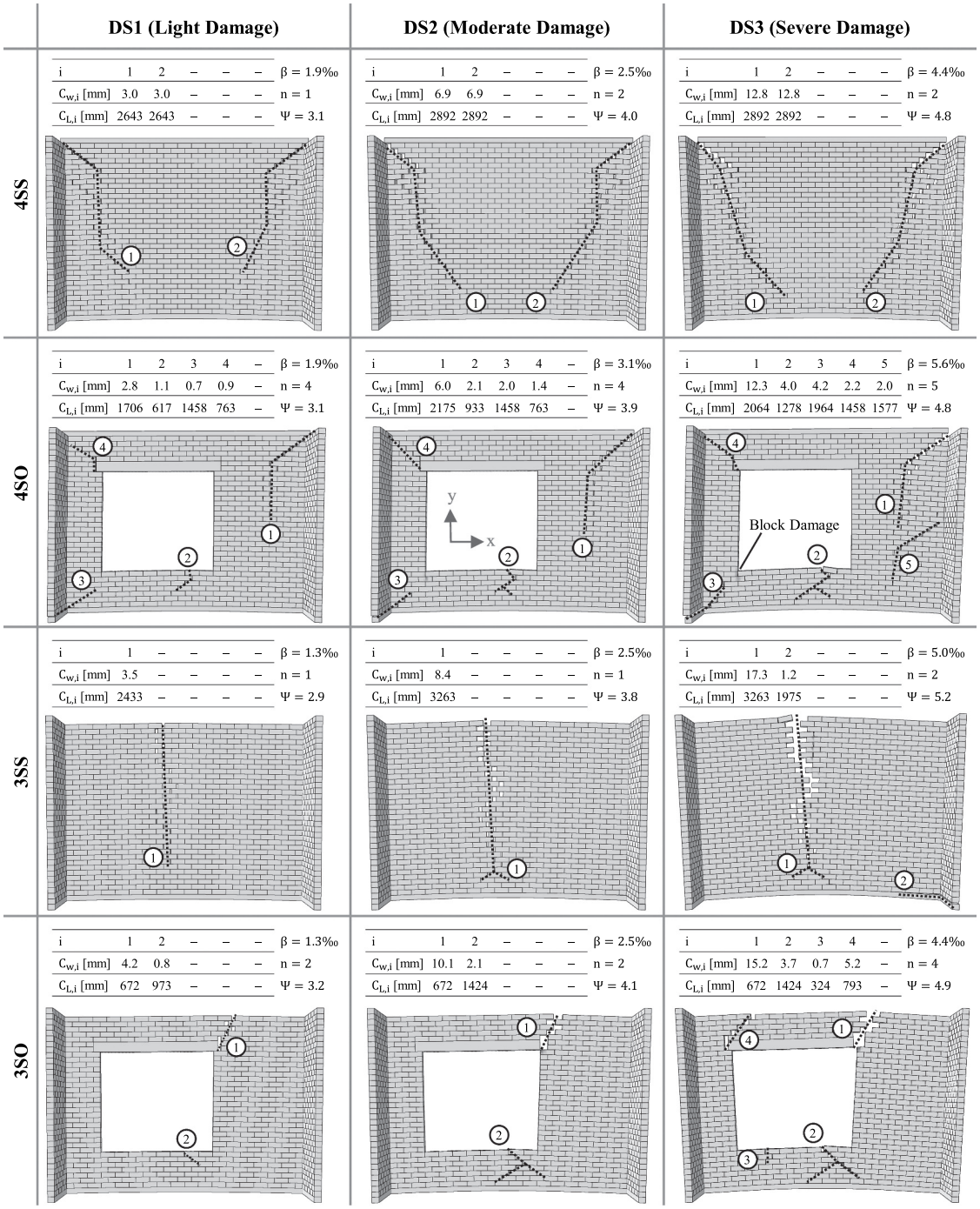

Figure 9. Damage states identified for wall specimens under symmetric hogging. Deformed shapes are × 20 magnified. Block damage (i.e., crushing or tensile cracking in units) is highlighted in red. The β is the value of "applied angular distortion" at which the damage state is identified.

piers. However, the 4SO wall under sagging shows delayed damage progression in the reversed asymmetric case, as it does not form a base crack.

The moments at which different pre-damage states are reached during settlement loading are shown in the angular distortion vs. IP drift curves in Figure 10. The drifts used to construct these curves are calculated as the maximum between the IP displacements at the two top corners of the main walls, divided by the height of the specimens (2575 mm). In the 4SS and 4SO specimens subjected to symmetric and asymmetric hogging, different pre-damage states are reached at similar IP drift levels. In these cases, the asymmetric hogging profile introduces an additional base crack, which compensates for its otherwise lower damaging nature compared to the symmetric profile. In contrast, the 3SS and 3SO

Table 3. Angular distortions corresponding to light- to severe-damage states of the specimens.

	Angular Distortion[a] [‰]											
	4SS			4SO			3SS			3SO		
Settlement Profile	DS1	DS2	DS3	DS1	DS2	DS3	DS1	DS2	DS3	DS1	DS2	DS3
Sym. Hog.	1.9	2.5	4.4	1.9	3.1	5.6	1.3	2.5	5.0	1.3	2.5	4.4
Asym. Hog.	3.8	6.9	14.4	4.4	8.8	12.5	3.1	6.3	11.3	1.9	3.8	7.5
Rev. Asym. Hog.	–	–	–	3.8	5.6	8.1	–	–	–	1.9	3.1	6.9
Asym. Sag.	5.0	8.8	18.1	2.5	6.3	13.1	5.0	8.8	18.1	2.5	5.6	11.9
Rev. Asym. Sag.	–	–	–	3.1	8.1	13.1	–	–	–	3.1	6.3	10.0

[a]These are the angular distortions applied to the base.

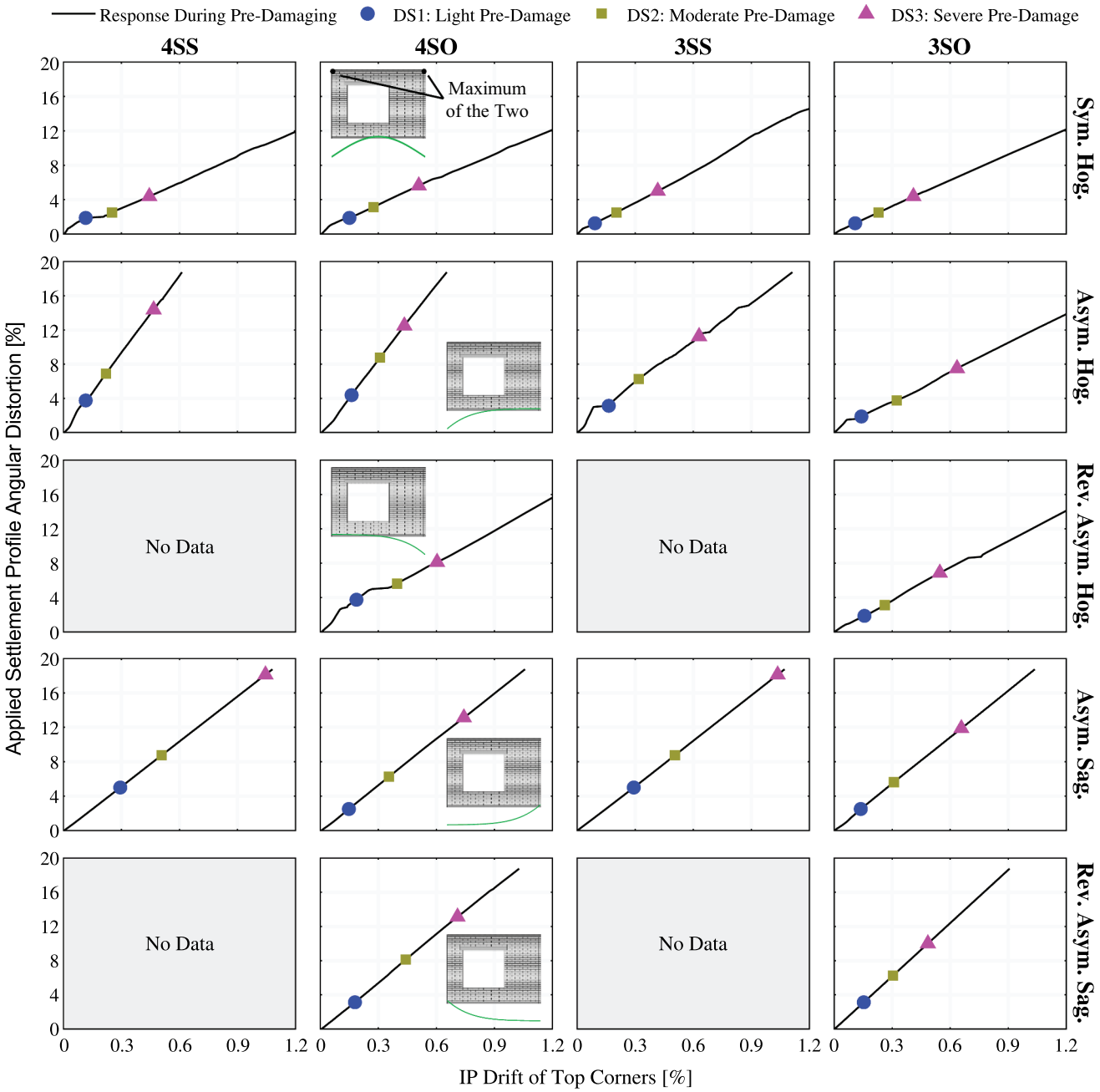

Figure 10. Evolution of top IP drift in different specimens during settlement pre-damaging.

specimens under asymmetric hogging require larger IP drifts to reach the same damage states, as this profile does not induce base cracking as prominently as in the 4SS and 4SO specimens. This response is further evidenced when comparing the response of the 4SO specimen under symmetric and asymmetric hogging: the asymmetric profile fails to initiate base cracking, and as a result, a larger IP drift is needed to reach DS3. Sagging profiles also require higher IP drifts to reach different pre-damage states, especially DS3, likely due to the concentration of cracking at the base of the walls. Notably, the 4SS and 3SS specimens reach DS3 under sagging at very large drift values (approximately 1%), as they do not develop additional cracks and instead deform in a more rigid manner. Conversely, the 3SO specimen under reversed asymmetric sagging reaches DS3 at a lower IP drift due to more distributed cracking across the main wall. Overall, the range of specimen geometries and settlement profiles considered in this study captures a wide variety of damage responses to settlement loading.

5.2. Modal analysis: effects of pre-damage on stiffness

The results of modal analyses on pristine specimens are presented in Figure 11, showing the modal shapes, natural frequencies, and participating mass factors for the first four natural vibration modes. The same boundary conditions as those used in the static OOP simulations are adopted (Figure 5b1). Following the approach in the previous study of the authors (Ghezelbash, Sharma, et al. 2025), the first and third modes, having the largest participating mass factors, are identified as the modes most likely to govern the OOP response and are selected for damping calibration in the expanded blocks. A target Rayleigh damping ratio of 5% is used, as described earlier in Section 2.4. This damping ratio is calibrated based on the modal properties of the pristine specimens. Thus, reductions in stiffness and natural frequency due to settlement-induced damage do not alter the computed values. This choice is made to streamline the analysis process and avoid introducing uncertainties associated with recalibrating damping for each pre-damage state. Moreover, damping is considered to have the most influence once a collapse mechanism has activated (i.e., beyond near collapse), a phase that is not the primary focus of this study. It should be noted that the combination of the lowest first-mode period of the specimens ($T = 1/32.02$ s in 4SO) and the $\Delta t_{max} = 0.0025$ s used in dynamic simulations leads to a $\Delta t_{max}/T = 8\%$ which completely prevents numerical energy dissipation.

The first-mode frequencies obtained from modal analyses on specimens at different pre-damage states are used to estimate changes in the OOP stiffness of the specimens due to settlement-induced pre-damage. Equation 2 is employed for this purpose, where K_{DSi} and f_{DSi} represent the OOP stiffness and first-mode frequency at pre-damage state DSi, respectively. This approach idealizes the specimens as a single-degree-of-freedom system wherein the relationship $f = \sqrt{K/m}$ can be used.

$$\frac{K_{DSi}}{K_{DS0}} = \left(\frac{f_{DSi}}{f_{DS0}}\right)^2 \tag{2}$$

The calculated changes in the OOP stiffness of pre-damaged specimens are presented in Figure 12, and the modal shapes belonging to their first deformation mode at DS1 are shown in Figure 13. A broad variability in stiffness sensitivity emerges, from low to moderate reductions of around 30% in the 3SS and 3SO specimens under hogging, and even very large reductions, up to 80–92%, in the 4SS and 4SO specimens under sagging at DS3. With respect to the influence of the settlement profile, all specimens exhibit the most pronounced stiffness reductions under sagging, being already noticeable at DS1. This response is attributed to the disruption of vertical arching caused by base cracking. The effect is especially significant in the 4SS and 4SO specimens, which exhibit reductions of 50–80% at DS1, due to the presence of the top beam and the larger vertical precompression. In other words, the more prominent the vertical arching in the pristine specimen, the greater the impact of its loss during sagging. The 3SS and 3SO specimens show lower stiffness reductions under sagging (up to 48% at DS1), which is associated with more distributed cracking. Nevertheless, even in these specimens, sagging has a greater impact on OOP stiffness than hogging. Despite having lower vertical confinement, the loss of support at one boundary under sagging shifts the OOP response of these specimens toward that of one-way horizontally spanning elements, rather than their original two-way spanning configuration (as further discussed in Section 5.3). In summary, these findings demonstrate that sagging, which is typically considered the less damaging settlement scenario due to its association with localized cracking (Burd et al. 2000), has a greater effect on the OOP stiffness of the specimens than hogging when it disrupts vertical arching, as in the specimens analyzed in this study.

Among the specimens subjected to hogging, 4SO shows substantial stiffness reduction, up to 60% at DS3 under symmetric settlement. This is attributed to the development of cracks beneath the window, which

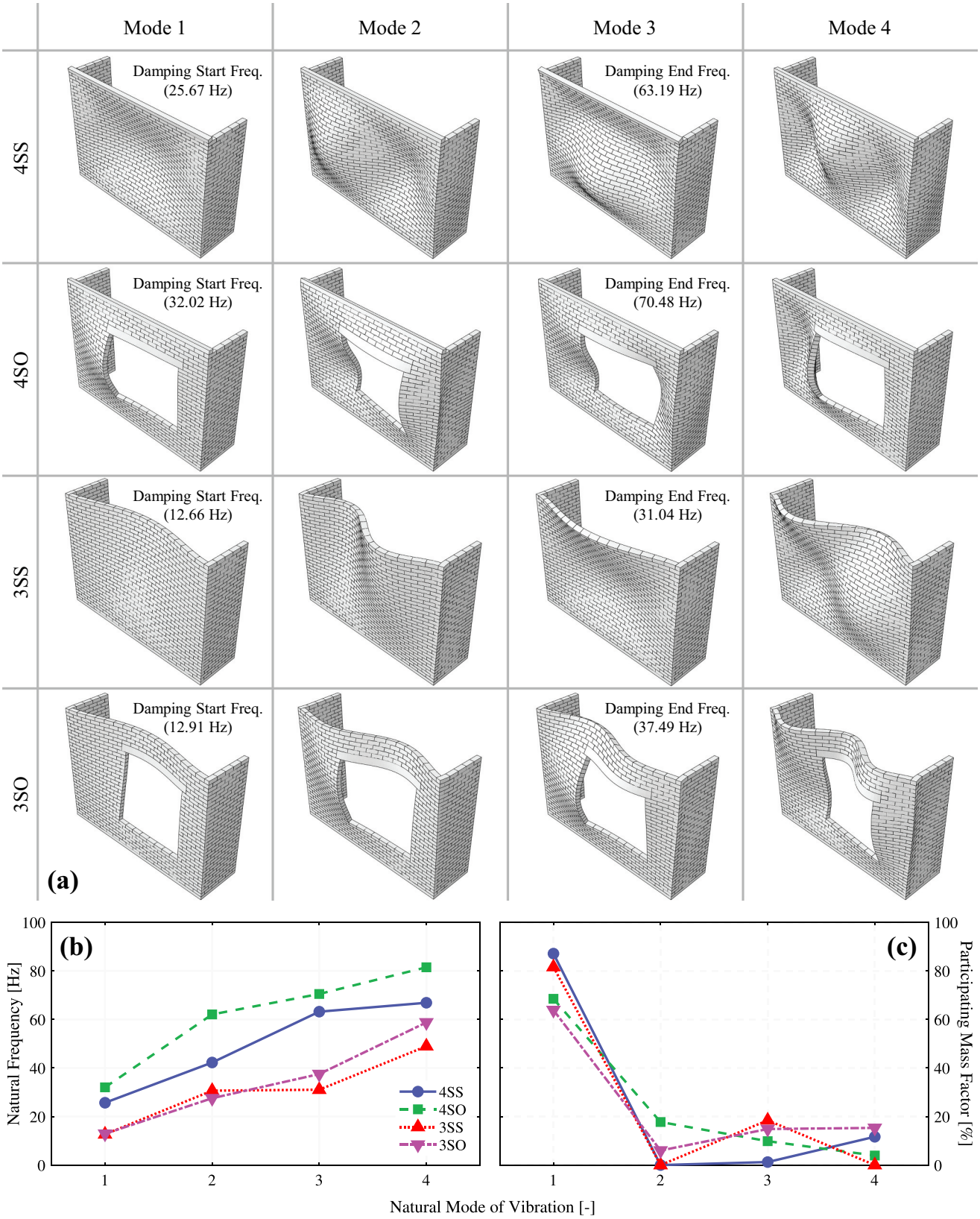

Figure 11. The results of the modal analysis of the pristine numerical specimens: modal shapes (a), frequencies (b), and participating mass factors (c) of the first four natural modes of vibration. Frequencies used to calibrate Rayleigh damping are shown in the deformed shapes.

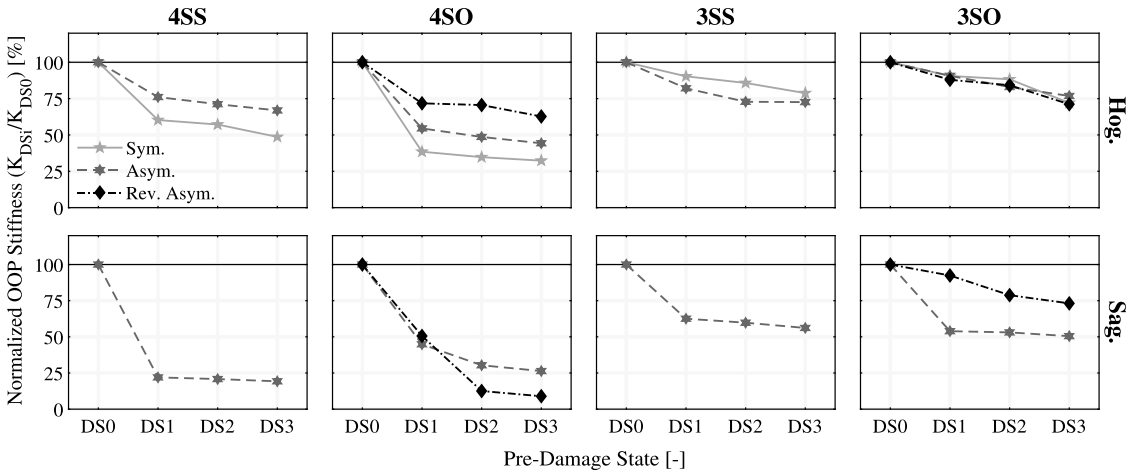

Figure 12. Changes in OOP stiffness of specimens as a result of settlement-induced pre-damage. The square of the ratio of first-mode-frequency in pre-damaged walls to that of the pristine walls is shown.

isolate the bottom spandrel from the rest of the main wall, allowing it to participate independently in modal deformations. The OOP analyses presented in Section 5.3 further illustrate the vulnerability of the spandrel in this configuration. With respect to the sensitivity to settlement profile symmetry, both the 4SS and 4SO walls exhibit 12–18% greater stiffness reduction under symmetric hogging compared to the asymmetric case, due to the more widespread cracking induced by the former. In contrast, the 3SS and 3SO specimens demonstrate lower sensitivity, as cracking patterns are less different between symmetric and asymmetric profiles. In fact, the 3SS specimen shows faster stiffness degradation during asymmetric hogging, due to the formation of an additional base crack in this scenario. With respect to the direction of the settlement profile, the sensitivity varies depending on boundary conditions and crack types. The 3SO specimen shows minimal sensitivity under hogging. However, the 4SO specimen displays a notable difference: asymmetric hogging results in 18% greater stiffness reduction at DS3 compared to the reversed asymmetric profile. This discrepancy is attributed to crack localization during asymmetric hogging, as well as the lower severity of the base crack under the reversed profile. A similar effect is observed in the 3SO specimen under sagging, where the reversed asymmetric profile does not induce base cracking and leads to a stiffness reduction at DS1 up to 40% lower than the original asymmetric case. Conversely, in the 4SO specimen, the reversed asymmetric sagging profile results in a 17% higher stiffness reduction at DS3. This is due to the formation of a horizontal crack extending from the window to the long pier, leading to its increased looseness during modal deformations.

In almost all specimens, the majority of the OOP stiffness reduction occurs upon reaching DS1. This is because most cracks form at this early stage, already disrupting vertical and horizontal confinement and compromising boundary support. Progression through higher pre-damage states results mainly in the widening of existing cracks and the formation of only a limited number of additional cracks, both of which contribute less significantly to further stiffness degradation. The stiffness sensitivities observed here are expected to strongly influence the dynamic response of the specimens: as pre-damage reduces natural frequencies (i.e., increases natural periods), the resonance of the specimen shifts to a different part of the acceleration spectrum of the loading signal. This shift may either increase or decrease the amplification of seismic motions experienced by the specimens, thereby influencing the extent to which their collapse PMAs change. These effects are further examined in Section 5.4.

5.3. Pushover analyses: effect of pre-damage on the static OOP performance

The results of the pushover and reversed pushover OOP analyses are presented and discussed in this section. The resulting force–displacement curves for all specimens under pushover and reversed pushover are shown in Figures 14 and 15, respectively. In these figures, each column of sub-figures corresponds to a specific specimen, while each row corresponds to a particular settlement profile. Within each sub-figure, all curves are normalized by the peak OOP resistance of the pristine configuration, denoted as $V_{max,DS0}$ and indicated within each sub-figure, to enable straightforward comparison

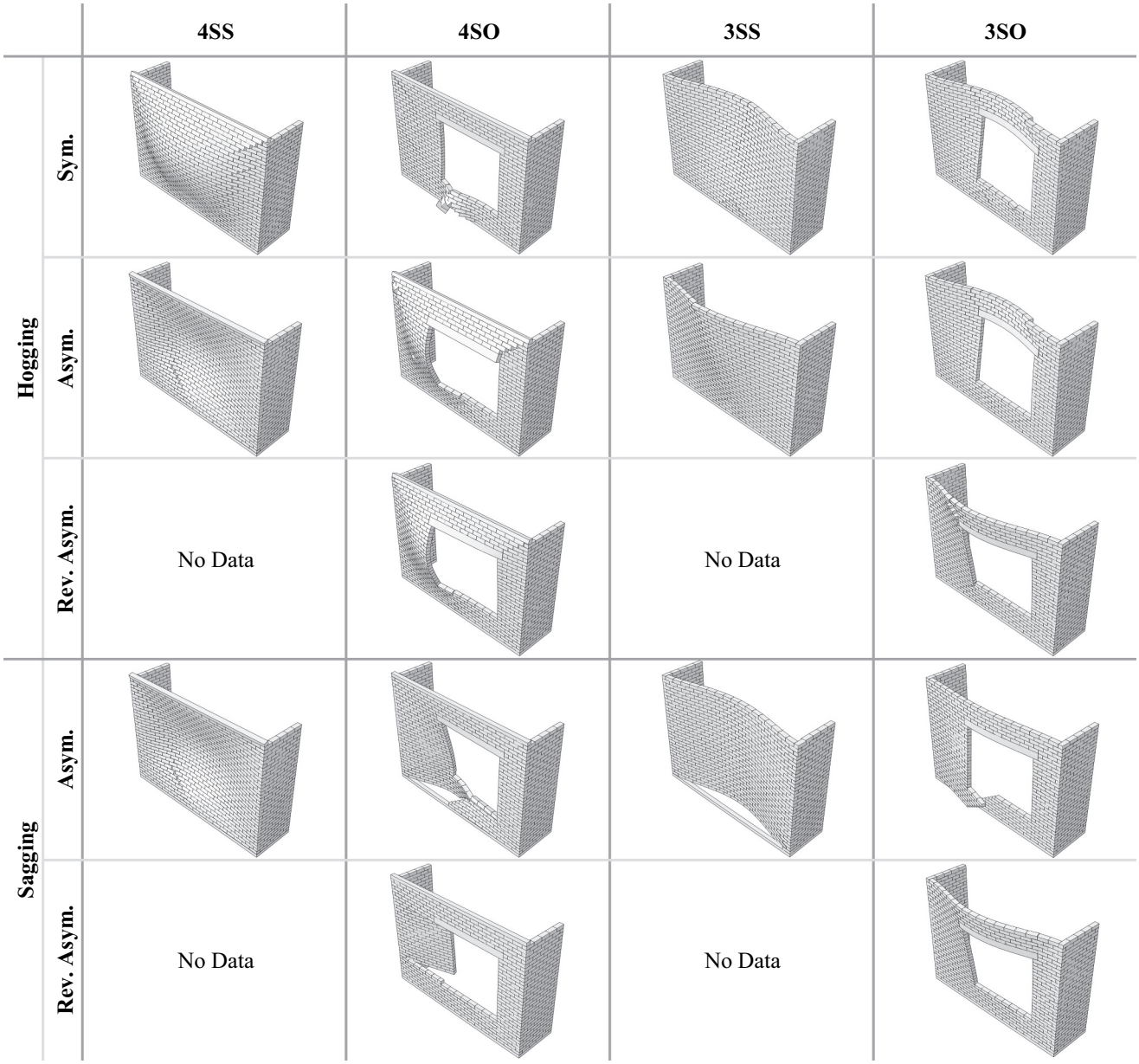

Figure 13. Modal shapes of first natural deformation modes in specimens at DS1 settlement-induced pre-damage state.

across different damage states. Additionally, $V_{max,DS0}$ is presented as a coefficient of the specimen weight (denoted as W) to facilitate comparison with dynamic collapse PMAs. Specimen weights exclude the base and top beam, and are 28.08 kN for the 4SS/3SS specimens and 23.16 kN for the 4SO/3SO specimens. Displacements are normalized relative to the main wall thickness (t = 102 mm). The peak OOP strength of the pre-damaged specimens under both pushover and reversed pushover is summarized in Figure 16, normalized by $V_{max,DS0}$. Figure 17 and Figure 18 show the corresponding damage patterns for DS1 specimens under pushover and reversed pushover loading, respectively. In these figures, damage in the blocks is highlighted in red, and different deformation scales are used to enhance visibility of crack patterns. The displacements used in the pushover curves are measured at specific control points indicated in Figure 17. For the 4SS and 3SS specimens, the control point is located at mid-length and mid-height of the main wall and at the top edge, respectively. For the 4SO specimen, the control point is located at the lintel height on the edge adjacent to the long pier. For the 3SO specimen, the control point is located at the top of the main wall, directly above the intersection of the lintel and the long pier. These same control points are used consistently for both pushover and reversed pushover analyses.

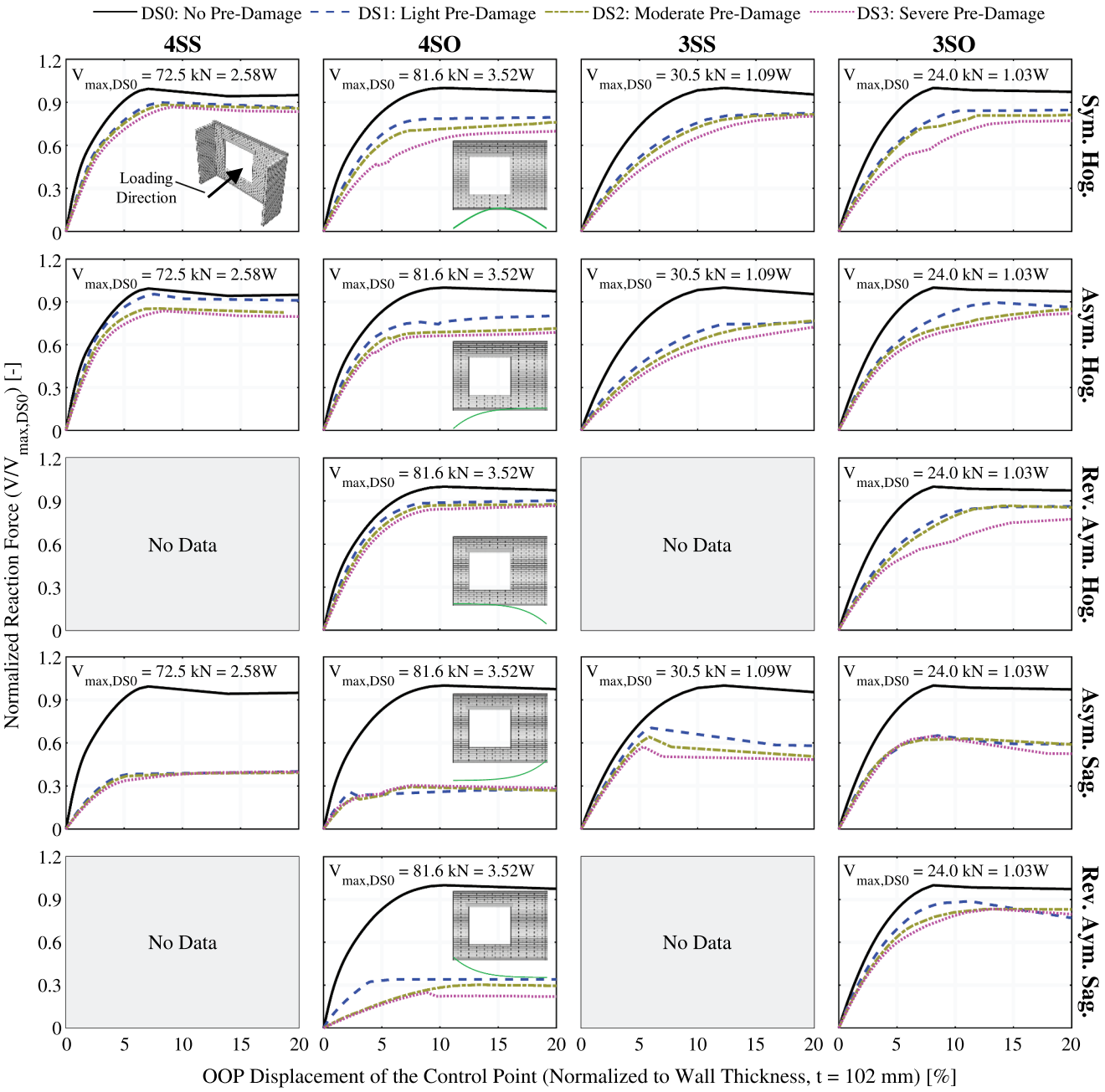

Figure 14. Force-displacement results of static pushover OOP analyses of specimens under settlement pre-damage. W is weight of the specimens, 28.08 kN for 4SS/3SS and 23.16 kN for 4SO/3SO.

Similar trends to those observed in the influence of settlement on OOP stiffness are identified when comparing OOP strengths and collapse failure mechanisms. First and most notably, the majority of strength reduction occurs already for pre-damaged walls at DS1, highlighting the significant impact of light pre-damage. In fact, the DS1 specimens exhibit the most substantial changes in collapse mechanisms compared to the pristine (DS0) walls, while further progression to higher pre-damage states results in only marginal additional modifications. It should be noted that, due to the absence of intermediate pre-damage states between DS0 and DS1, the precise onset of strength degradation cannot be identified. Further investigation into the OOP response of URM walls under finer levels of light pre-damage (such as negligible, very slight, and slight categories as defined in (Prosperi 2025)) is required to more accurately identify this transition point.

Second, sagging leads to greater strength loss across all specimens, particularly in 4SS and 4SO, resulting in strength reductions of 50–85% at DS3. This further emphasizes the critical role of the base

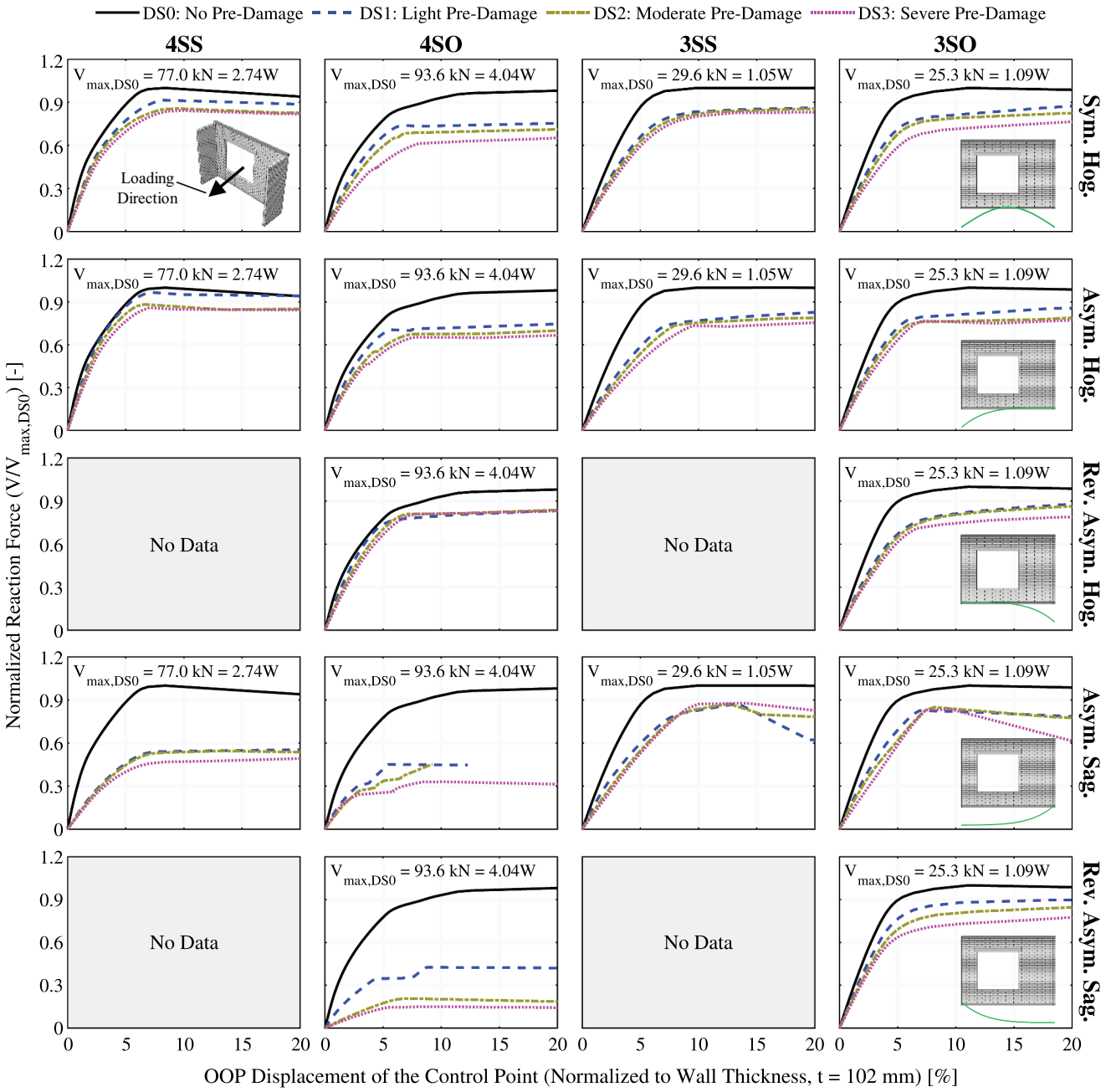

Figure 15. Force-displacement results of static reversed pushover OOP analyses of specimens under settlement pre-damage. W is weight of the specimens, 28.08 kN for 4SS/3SS and 23.16 kN for 4SO/3SO.

crack induced by sagging. In these specimens, even DS1 results in the loss of base support, which subsequently triggers the formation of one-way bending cracks in the lower portion of the main wall. A similar effect is observed in the 3SS specimen under regular pushover (Figure 17), where a 40% strength loss occurs at DS1. However, the impact is less pronounced in this case, as the DS0 failure mechanism already exhibits a one-way spanning response due to the absence of vertical confinement. Once more, it should be noted that the sagging profile used in this study represents an extreme case. In real-world conditions, settlement profiles typically exhibit lower curvature and do not induce base cracking to the same extent as those modeled here. Additionally, the specimens used in this study have relatively short lengths compared to actual building façades (Prosperi et al. 2023b). This leads to higher horizontal confinement, causing the walls to deform more rigidly under sagging and limiting the formation of internal cracks that might otherwise reduce the severity of base cracking.

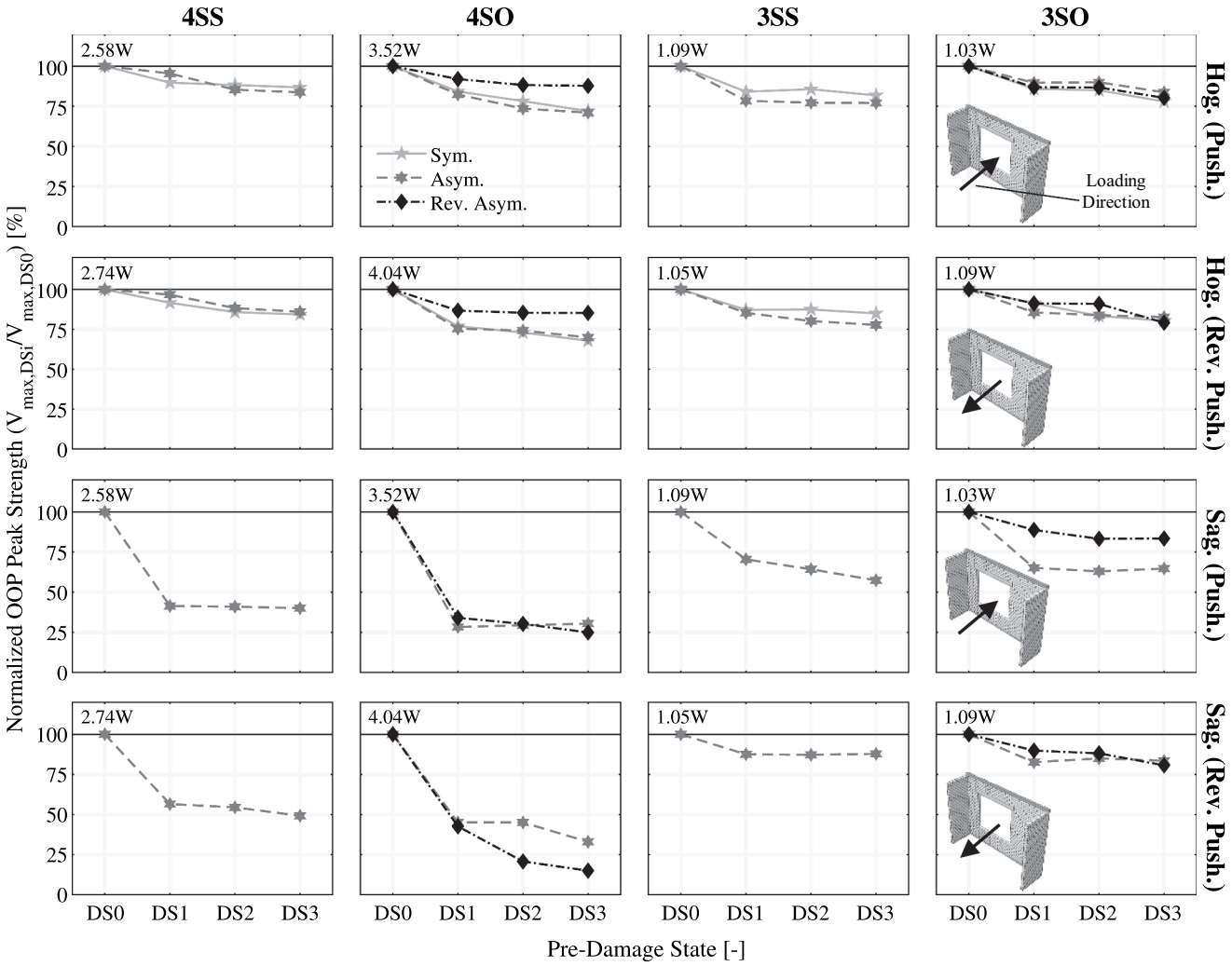

Figure 16. Changes in static pushover OOP strength of specimens as a result of settlement-induced pre-damage. Peak strengths are normalized to those of pristine specimens. W is weight of the specimens, 28.08 kN for 4SS/3SS and 23.16 kN for 4SO/3SO.

Third, the 4SO wall under hogging exhibits a significant 30% strength reduction, particularly under reversed pushover. This is primarily attributed to the looseness and partial collapse of the bottom spandrel. Fourth, the remaining specimens under hogging demonstrate relatively lower sensitivity to pre-damage, with strength losses of up to 23% at DS3. This reduced sensitivity is due to the limited influence of settlement-induced pre-damage on their OOP failure mechanisms, as well as on their horizontal and vertical confinement. In specimens such as 3SS and 3SO, settlement causes only minor alterations in the collapsing wall region and does not significantly affect the force required to induce collapse.

The influence of the shape of settlement profile is less pronounced when comparing OOP strengths than in the case of OOP stiffness. Across all specimens, symmetric hogging results in strength reductions similar to those caused by asymmetric profiles. Likewise, the direction of asymmetry in the settlement profile leads to only minor differences in strength loss. In the 4SO specimen under asymmetric hogging, the reversed profile results in a 15% lower strength reduction at DS3, attributed to the increased stability of the bottom spandrel. For the 3SO specimen, the only notable difference is observed during sagging under regular pushover, where the reversed asymmetric settlement profile leads to a 20% lower strength drop at DS3 due to the absence of a base crack. The effects of loading direction are primarily observed in specimens subjected to sagging. Regular pushover, applied in the weak direction (away from the flanges), produces greater strength losses, particularly in 3SS and 3SO specimens. This is due to faster damage development at the wall-flange intersections. It is also observed that the 4SO specimen shows a 13% lower pristine OOP strength under regular pushover compared to reversed pushover, primarily due to the instability of the lintel. In contrast, the 4SS specimen

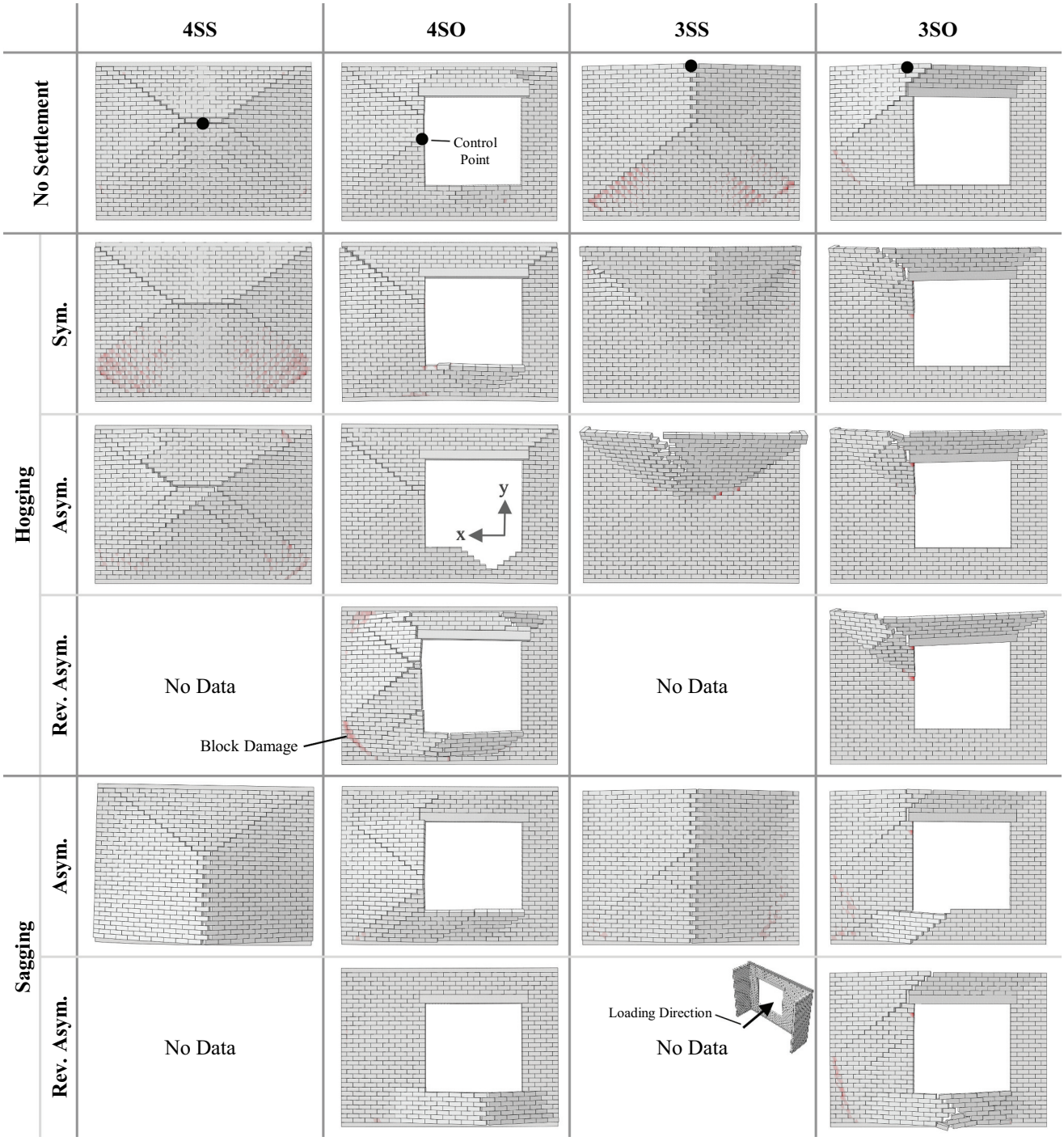

Figure 17. Damage patterns from static pushover OOP analyses of specimens under no pre-damage and DS1 settlement pre-damage. Damage in blocks (crushing or tensile cracking) is highlighted in red. Deformed shapes are scaled with different factors for clear visualization.

shows only a 6% difference, and the remaining two specimens exhibit no significant discrepancy. These results suggest that, while directional sensitivity in OOP strength is minor under pristine conditions, it becomes more pronounced following settlement-induced pre-damage, especially that caused by sagging.

5.4. Dynamic analyses: effect of pre-damage on the dynamic OOP performance and comparison with pushover analyses

The results of the dynamic IDAs using the induced and tectonic seismicity signals described in Section 4.4 are presented and discussed in this section. It should first be noted

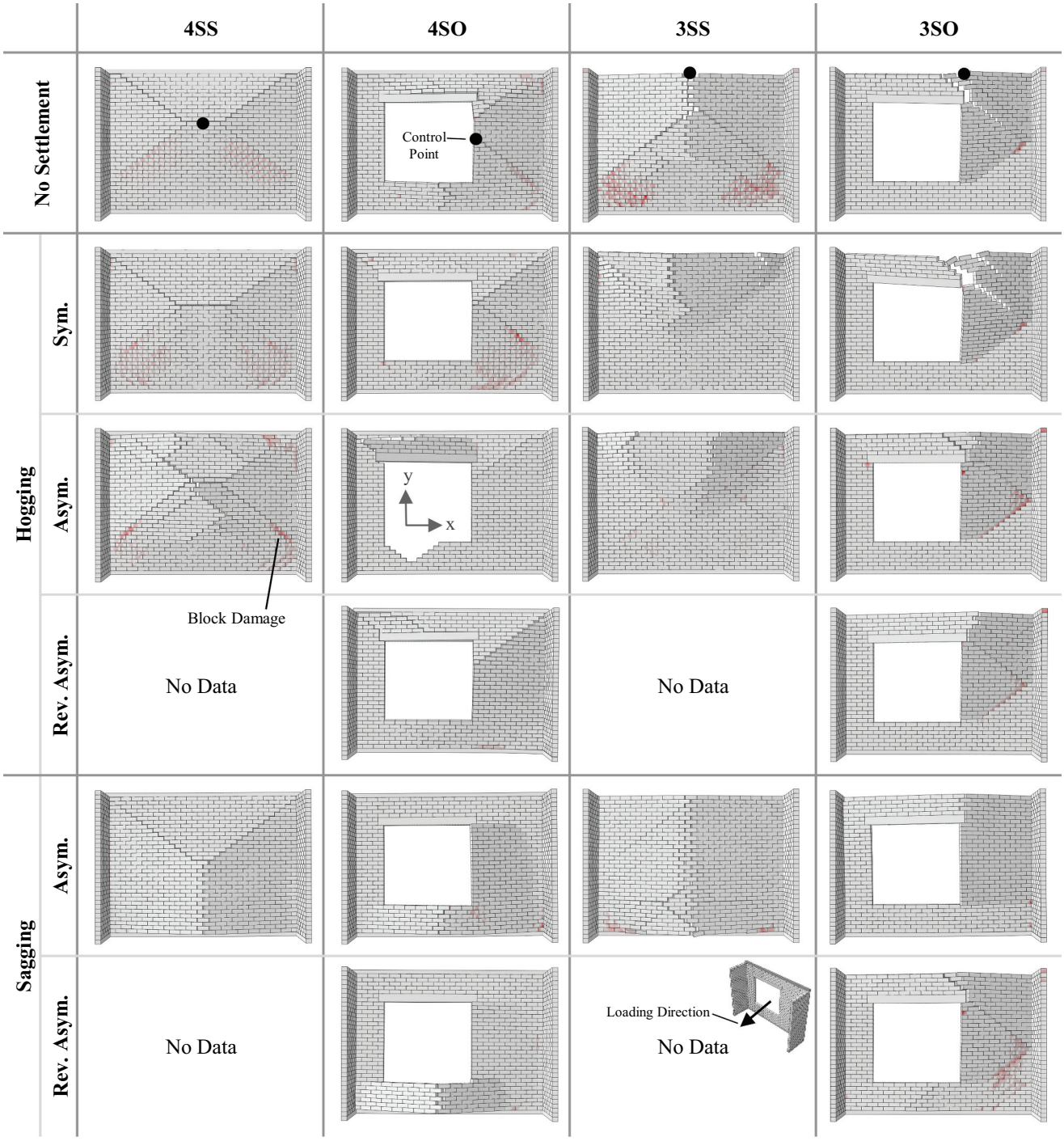

Figure 18. Damage patterns from static reversed pushover OOP analyses of specimens under DS1 settlement pre-damage. Damage in blocks (crushing or tensile cracking) is highlighted in red. Deformed shapes are scaled with different factors for clear visualization.

that none of the specimens collapsed under the induced seismicity signal within the loading intensities considered in this study. Therefore, the discussion focuses exclusively on the results from the tectonic signal analyses. The collapse PMAs are summarized in Table 4, and the corresponding failure mechanisms are illustrated in Figure 19. The control points used to identify the loading steps leading to collapse are the same as those used for the pushover analyses and are also indicated in Figure 19. The deformed shapes correspond to time steps that most clearly reveal the extent and location of damage. All dynamic collapses are identified using the 25% wall thickness deformation threshold defined in Section 4.4. However, it is worth noting that during the collapse simulations, the specimens reached substantially higher peak OOP deformations, up to 50% of the wall thickness, confirming the appropriateness of the

Table 4. Collapse PMAs of specimens under tectonic-seismicity IDAs.

	Collapse PMA[a] [g]											
	4SS			4SO			3SS			3SO		
Settlement Profile	DS0	DS1	DS3	DS0	DS1	DS3	DS0	DS1	DS3	DS0	DS1	DS3
Asym. Hog.	3.0	3.0	2.5	4.0	3.5	3.0	1.0	1.0	0.75	1.25	1.25	1.25
Rev. Asym. Hog.	3.0	–	–	4.0	3.5	3.5	1.0	–	–	1.25	1.25	1
Asym. Sag.	3.0	1.0	1.0	4.0	1.25	1.25	1.0	0.75	0.75	1.25	1.0	1
Rev. Asym. Sag.	3.0	–	–	4.0	1.25	1.0	1.0	–	–	1.25	1.25	1

[a]Peak motion acceleration causing physical collapse or OOP deformations exceeding 25% of thickness.

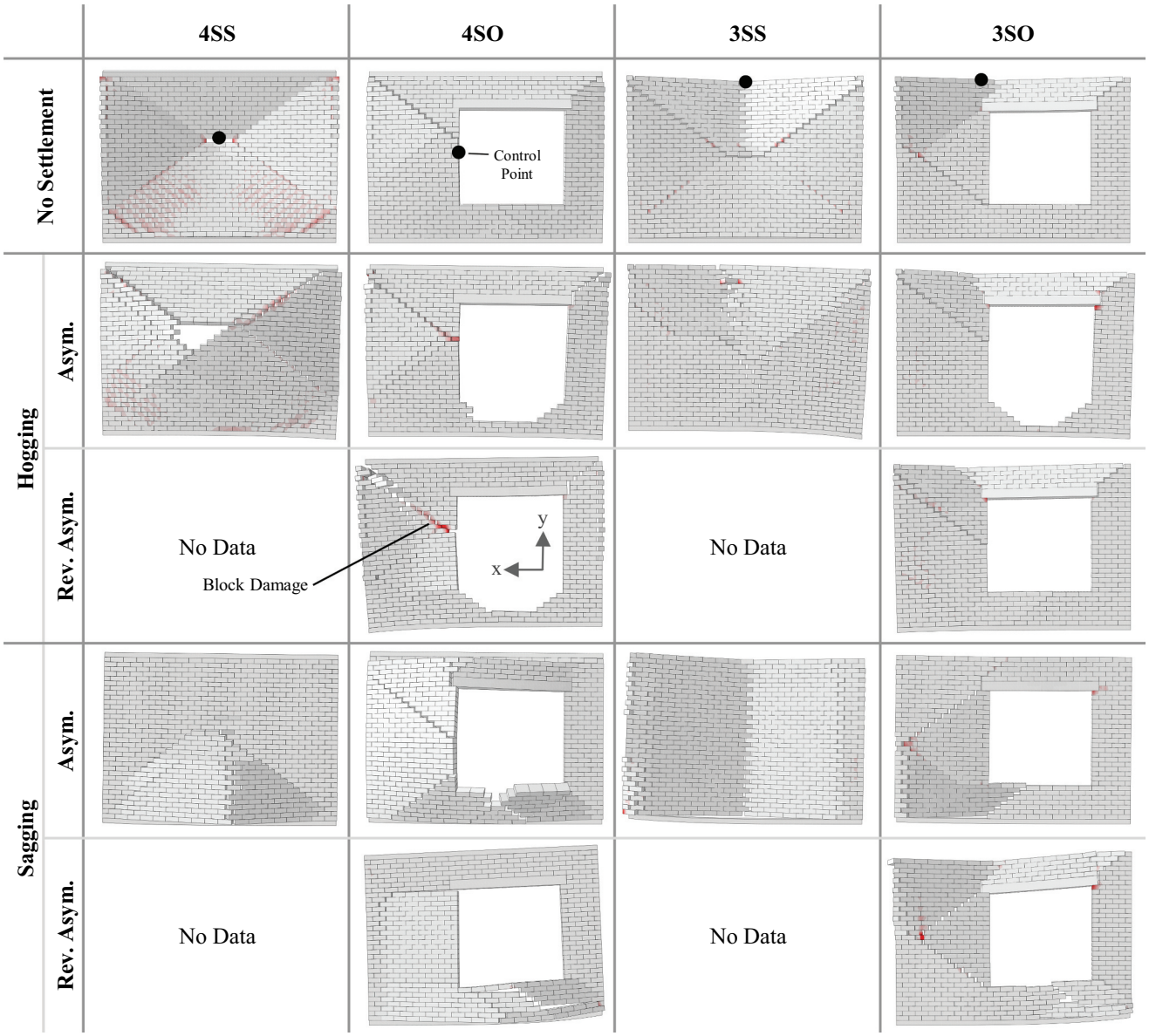

Figure 19. Damage patterns from IDA of specimens under DS1 settlement pre-damage and tectonic seismicity. Damage in blocks (crushing or tensile cracking) is highlighted in red. Deformed shapes are scaled with different factors for clear visualization.

collapse detection criterion. In summary, the same trends previously discussed, namely the significant drop in collapse PMA at DS1 and the severe impact of sagging, are also observed in the dynamic IDAs. Given the detailed discussion of these effects in previous sections, they are not repeated here. Instead, the focus is shifted toward comparing the dynamic response of the specimens with their response under static loading.

Figure 20 compares the changes in dynamic collapse PMAs with the strength reduction estimations obtained

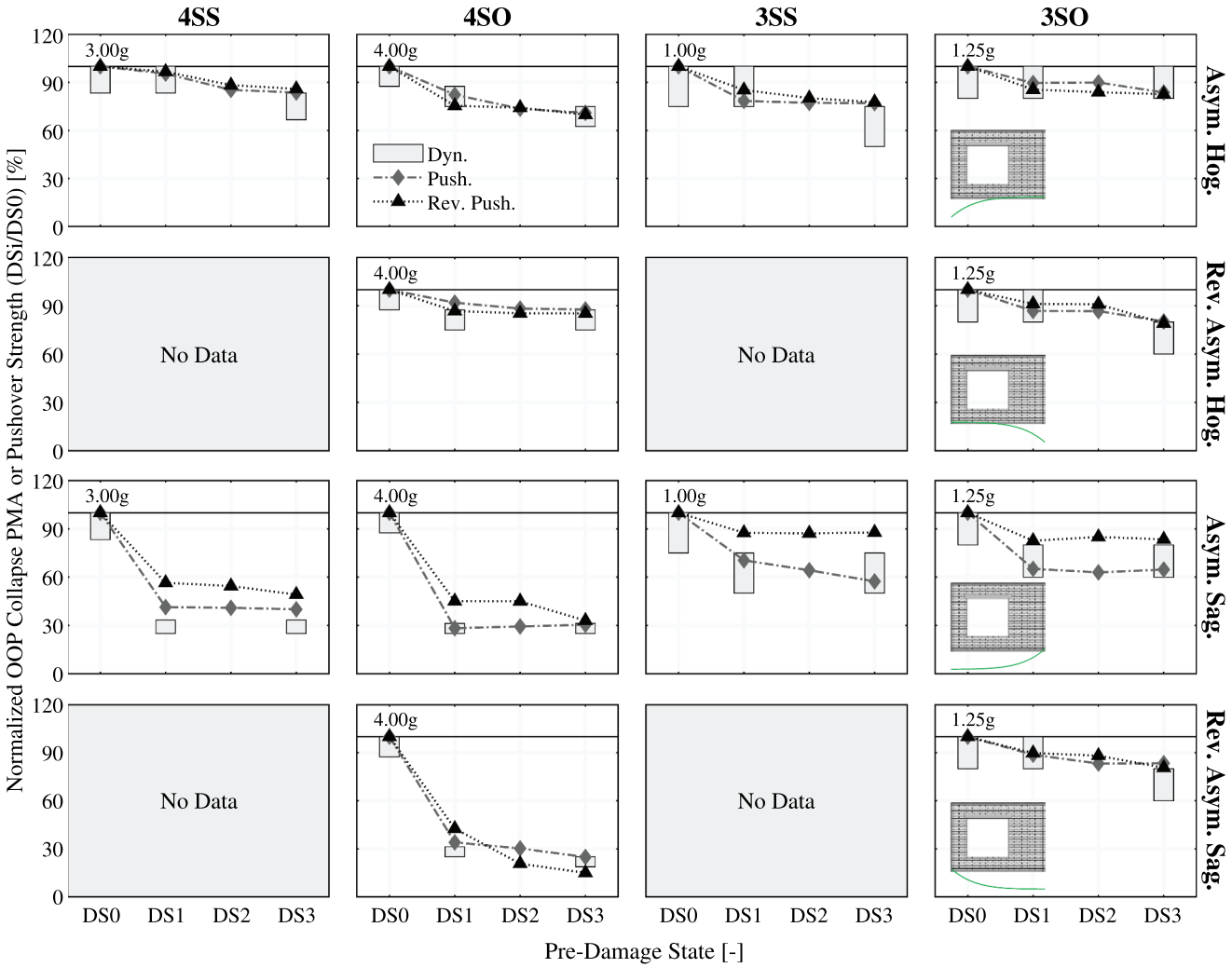

Figure 20. Comparison of strength drops predicated via dynamic (tectonic-seismicity) and pushover analyses for specimens under settlement pre-damage. Dynamic analysis results are shown as a range of expected collapse PMAs between the numerically obtained value and one loading intensity below it.

from the static analyses. A limitation arises because the static analyses apply a continuous load, whereas the IDAs are conducted using a predefined list of discrete loading intensities. As a result, although an estimated collapse PMA is determined, finer increments in loading intensity would be required to obtain an exact value (Ghezelbash, Sharma, et al. 2025). To address this limitation, the comparison does not rely on the exact numerical drop in collapse PMAs for pre-damaged specimens. Instead, a range is defined for each predicted dynamic collapse PMA. This range spans from the discretely identified collapse PMA to the loading intensity immediately below it in the IDA sequence.

Overall, excellent agreement is observed between the static and dynamic predictions, both in terms of the drop in OOP resistance and the failure mechanisms of the pre-damaged specimens. Particularly, the strength predicted via pushover analyses conducted in the weak direction (dashed-dotted lines with diamond markers in Figure 20) either falls within the range yielded by the dynamic analyses or matches the upper-bound of the predicted collapse PMA drops. The only exception is the 4SS specimen under sagging, which shows a slightly larger drop in collapse PMA (8%) across different pre-damage states. However, this discrepancy is considered negligible given the severity of the applied settlement profile. It is also worth noting that pushover analyses accurately estimate the strength of the pristine specimens: the ratio of pushover strength to specimen weight aligns well with the corresponding acceleration intensities. Such strong agreement is attributed to the nature of the OOP response studied herein: as two-way spanning walls predominantly exhibit force-controlled failure mechanisms (Sharma et al. 2020), similar outcomes from static and dynamic analyses are expected.

It should be noted that the results of this study are to be regarded as preliminary indicators, warranting

further investigation. In particular, the use of a single loading signal applied in a prescribed direction (Koc et al. 2023), as well as the specific material properties considered (Jafari 2021), may have introduced a degree of dependence of the outcomes on the specific setup of the parametric analysis. Additionally, the results of the dynamic simulations may have been influenced by the selected damping ratio. Notably, lower damping values may have resulted in reduced OOP strengths (Ghezelbash, Sharma, et al. 2025). However, such effects are not explored herein due to time constraints and the absence of a real-world benchmark for the studied specimens. As such, selecting a more appropriate damping ratio is not feasible, and any repetition of the analyses with altered damping would constitute a purely numerical variation. Further research is necessary to investigate the potential influence of these parameters. Nevertheless, it is important to note that while damping may affect the absolute OOP resistance of the specimens, the relative changes in strength due to pre-damage are expected to remain consistent with the trends observed in this study.

The pushover analyses, particularly those conducted in the weak direction, also demonstrate high accuracy in capturing the collapse mechanisms observed during dynamic simulations. A comparison between Figures 17 and 19 reveals that all dynamically induced cracks align closely with those identified in the static pushovers. The only notable discrepancy appears in the 3SO specimens under sagging, where an additional diagonal crack extending from the bottom corner of the window to the mid-height of the long pier emerges during dynamic loading. However, this damage pattern is also captured in the reversed pushover simulations (see Figure 18), suggesting that the static approach nevertheless encompasses the critical failure modes.

An appealing aspect of static analyses observed here is their relatively low computational demand compared to IDAs. As an example, while each loading run of the tectonic IDA of the pristine 4SS specimen requires a computational time similar to that of its static analysis (2.4 vs 2 hours on 16 CPU cores @ 4.2 GHz clock speed), the complete IDA of the wall, consisting of nine analyses with PMAs ranging from 0.75 g to 4 g, takes approximately 980% longer (approximately 22 hours). Although, this difference is significantly smaller for walls with lower dynamic collapse PMAs, such as the 3SS specimens under DS3 pre-damage which collapse in their first dynamic loading run at a PMA of 0.75 g.

Overall, these comparisons indicate that, at least within the context and limitations of this study, static analyses can serve as reliable and efficient tools for predicting the seismic OOP response of both pristine and settlement-damaged non-framed URM walls. Pushover analyses conducted in the weak direction of the specimens, in particular, provide accurate, and in some cases slightly conservative, estimates of structural capacity and failure mechanisms. It should be noted that pushover analyses retain some limitations in capturing specific dynamic effects, such as relative support motions governing the response of upper-floor walls and gables (Godio and Beyer 2019; Sharma et al. 2025). Hence, the use of dynamic analyses remains necessary when investigating these more complex response mechanisms.

As previously discussed, induced seismicity, scaled up to a loading intensity of 0.75 g, does not lead to damage sufficient to compromise the wall structural integrity. Even the 3SS specimen, despite reaching a collapse PMA of 0.75 g at DS3, only collapses under the tectonic seismicity signal. On one hand, this outcome suggests that under induced seismicity the influence of settlement pre-damage on the response of URM walls may be limited, particularly considering the extreme settlement scenarios considered in this study. On the other hand, the higher sensitivity observed under tectonic loading may be attributed to the characteristics of the loading signal, namely, its higher spectral accelerations and multiple accelerogram peaks. These findings underscore the need for further comparisons between the effects of induced and tectonic seismicity hazards.

6. Conclusions

This study investigates the effects of settlement-induced pre-damage on the seismic out-of-plane (OOP) response of non-framed unreinforced masonry (URM) walls. The block-based numerical modeling approach previously developed by the authors is adopted in a parametric analysis to explore these interactions. Four two-way spanning wall geometries are considered, including variations with window openings and free top edges, all representative of the URM building stock in the Groningen province of Netherlands. Each wall is subjected to different settlement profiles: symmetric and asymmetric hogging, asymmetric sagging, and reversed asymmetric hogging and sagging. During settlement loading, performance states, termed pre-damage states, are identified based on the severity of cracking and used as initial conditions for subsequent OOP analyses. These states represent light, moderate, and severe pre-damage conditions. Static pushover OOP analyses are performed in two opposite directions to account for the asymmetric geometry of the specimens. Incremental dynamic OOP analyses are also conducted using two seismic loading signals: one

representing induced seismicity and the representing from a tectonic earthquake. In addition, frequency analyses are carried out on the pre-damaged specimens prior to OOP loading. The results are interpreted in terms of changes in OOP stiffness (deduced from changes in fundamental frequencies), strength, and failure mechanism resulting from different pre-damage levels, as well as the influence of dynamic loading on the extent of these changes. The main outcomes of the study are as follows:

- The specimens exhibit significant sensitivity to sagging, with stiffness losses reaching up to 92% and strength reductions up to 85% at severe pre-damage states. This response is primarily attributed to the loss of vertical confinement and base support, which causes the walls to shift from their original two-way bending response to a one-way horizontal OOP bending mechanism.
- Hogging results in lower, yet still significant, degradation of OOP response. Specimens with vertical confinement experience up to 60% stiffness loss and 30% strength reduction at severe pre-damage states. The specimen with an opening is particularly vulnerable due to damage localization beneath the window, leading to looseness and early detachment in that region.
- The direction of settlement asymmetry also influences the response, particularly in specimens subjected to hogging. Settlement profiles that induce the opening of a base crack lead to a significantly greater impact, up to 40% larger stiffness reduction and 20% greater strength loss, due to the associated loss of base support and vertical confinement.
- The primary effects of settlement-induced pre-damage, both quantitatively and qualitatively, emerge as soon as the wall is subjected to light pre-damage state. Further progression to more severe damage states results in only minor additional changes to OOP strength, stiffness, and collapse mechanisms.
- Dynamic loading using an induced seismicity signal, scaled up to an intensity of 0.75 g, does not cause collapse in any specimen. In contrast, some severely pre-damaged specimens collapse under the same intensity when subjected to the tectonic signal, likely due to higher spectral accelerations and multiple strong motion peaks of the latter.
- Pushover analyses accurately estimate both the dynamic OOP strength of pristine walls and the strength reductions due to different levels of pre-damage. They also successfully capture the dynamic collapse mechanisms. This agreement is likely due to the force-controlled nature of the two-way OOP bending responses examined in this study.

This study provides key insights into the influence of settlement-induced pre-damage on the seismic OOP response of URM walls. However, further research is needed to refine and expand on these limited findings. Future studies should explore larger wall assemblies or full façades with more complex geometries and greater lengths, as well as implement more realistic settlement profiles with lower curvatures. These could include repeated settlement and uplift cycles to reflect actual field conditions more accurately. Additionally, alternative material configurations, such as combinations of weak units and strong mortars, should be investigated. Furthermore, walls with lower and higher overburdens should be studied. In this regard, this study establishes a framework for future studies rather than providing definitive conclusions. For example, while the current findings suggest that settlement pre-damage may have limited impact under induced seismicity, this conclusion is specific to the selected loading signals and scenarios. Broader dynamic analyses using diverse seismic records are necessary to generalize the results. Moreover, the reliability of static pushover analyses in predicting the seismic response of URM walls requires further verification by analyzing one-way spanning walls. Also, the influence of various levels of light pre-damage (e.g., Negligible, Very Slight, and Slight per EMS-98) on the OOP response warrants further investigation to better define the onset of pre-damage effects. Finally, future studies should design reinforcement or retrofitting techniques capable of mitigating the effects of settlement pre-damage on the seismic response.

Acknowledgement

The loading signals used for the dynamic simulations of this study are adapted from the experimental campaign conducted at EUCENTRE foundation (Pavia, Italy) on full-scale URM buildings (Miglietta et al. 2021; Graziotti et al. 2017).

Author contributions

CRediT: **Amirhossein Ghezelbash:** Conceptualization, Data curation, Formal analysis, Investigation, Methodology, Resources, Software, Validation, Visualization, Writing – original draft, Writing – review & editing; **Alfonso Prosperi:** Conceptualization, Methodology, Validation, Writing – review & editing; **Satyadhrik Sharma:** Conceptualization, Funding acquisition, Methodology, Supervision, Validation, Writing – review & editing; **Antonio Maria D'Altri:** Conceptualization, Funding acquisition, Methodology, Supervision, Validation, Writing – review & editing; **Jan G. Rots:** Conceptualization, Funding acquisition, Methodology, Resources, Supervision, Validation, Writing – review & editing; **Francesco Messali:** Conceptualization, Funding

acquisition, Methodology, Project administration, Resources, Supervision, Validation, Writing – review & editing.

Disclosure statement

No potential conflict of interest was reported by the author(s).

Funding

This research was conducted as part of the scientific consolidation of projects funded by Nederlandse Aardolie Maatschappij (NAM) BV under contract number UI46268 "Physical testing and modeling–Masonry structures Groningen", which is gratefully acknowledged. This work was partially supported by ReLUIS and Italian Department of Civil Protection, as part of the activity was carried out in the framework of the ReLUIS-DPC Project 2024–2026 Work Package 10 (Masonry structures), Task 10.1.

ORCID

Francesco Messali http://orcid.org/0000-0002-5525-8522

Data availability statement

The datasets generated during the current study are available from the corresponding author, AG, upon reasonable request.

References

Ancheta, T. D., R. B. Darragh, J. P. Stewart, E. Seyhan, W. J. Silva, B. S. J. Chiou, K. E. Wooddell, et al. 2014. "NGA-West2 Database." *Earthquake Spectra* 30 (3): 989–1005. https://doi.org/10.1193/070913EQS197M

Beyer, K. 2012. "Peak and Residual Strengths of Brick Masonry Spandrels." *Engineering Structures* 41:533–547. https://doi.org/10.1016/j.engstruct.2012.03.015

Billio, M., M. Costola, L. Pelizzon, and M. Riedel. 2022. "Buildings' Energy Efficiency and the Probability of Mortgage Default: The Dutch Case." *The Journal of Real Estate Finance & Economics* 65 (3): 419–450. https://doi.org/10.1007/s11146-021-09838-0

Boelhouwer, P., and H. van der Heijden. 2018. "The Effect of Earthquakes on the Housing Market and the Quality of Life in the Province of Groningen, the Netherlands." *Journal of Housing and the Built Environment* 33 (2): 429–438. https://doi.org/10.1007/s10901-018-9600-y

Bojadjiev, J., R. Apostolska, G. Necevska Cvetanovska, D. Varevac, and J. Bojadjieva. 2025. "Experimental Verification of Innovative, Low-Cost Method for Upgrading of Seismic Resistance of Masonry Infilled RC Frames." *Applied Sciences* 15 (15): 8520. https://doi.org/10.3390/app15158520

Bommer, J. J., P. J. Stafford, E. Ruigrok, A. Rodriguez-Marek, M. Ntinalexis, P. P. Kruiver, B. Edwards, B. Dost, and J. van Elk. 2022. "Ground-Motion Prediction Models for Induced Earthquakes in the Groningen Gas Field, the Netherlands." *Journal of Seismology* 26 (6): 1157–1184. https://doi.org/10.1007/s10950-022-10120-w

Boscardin, M. D., and E. J. Cording. 1989. "Building Response to Excavation-Induced Settlement." *Journal of Geotechnical Engineering* 115 (1): 1–21. https://doi.org/10.1061/(ASCE)0733-9410(1989)115:1(1)

Bucx, T. H. M., C. J. M. van Ruiten, G. Erkens, and G. de Lange. 2015. "An Integrated Assessment Framework for Land Subsidence in Delta Cities." *Proceedings of the International Association of Hydrological Sciences* 372:485–491. https://doi.org/10.5194/piahs-372-485-2015

Bui, T. T., A. Limam, V. Sarhosis, and M. Hjiaj. 2017. "Discrete Element Modelling of the In-Plane and Out-of-Plane Behaviour of Dry-Joint Masonry Wall Constructions." *Engineering Structures* 136:277–294. https://doi.org/10.1016/j.engstruct.2017.01.020

Burd, H. J., G. T. Houlsby, C. E. Augarde, and G. Liu. 2000. "Modelling Tunnelling-Induced Settlement of Masonry Buildings." *Proceedings of the Institution of Civil Engineers - Geotechnical Engineering* 143 (1): 17–29. https://doi.org/10.1680/geng.2000.143.1.17

Burd, H. J., W. N. Yiu, S. Acikgoz, and C. M. Martin. 2022. "Soil-Foundation Interaction Model for the Assessment of Tunnelling-Induced Damage to Masonry Buildings." *Tunnelling and Underground Space Technology* 119:104208. https://doi.org/10.1016/j.tust.2021.104208

Burland, J. B., B. B. Broms, and V. F. B. De Mello. 1977. "Behaviour of Foundations and Structures." 9th International Conference on Soil Mechanics and Foundation Engineering, Tokyo, Japan.

Burland, J. B., and C. P. Wroth. 1975. *Settlement of Buildings and Associated Damage*. Hertsford, England: Building Research Station.

Burton, H. V., and G. G. Deierlein. 2018. "Integrating Visual Damage Simulation, Virtual Inspection, and Collapse Capacity to Evaluate Post-Earthquake Structural Safety of Buildings." *Earthquake Engineering and Structural Dynamics* 47 (2): 294–310. https://doi.org/10.1002/eqe.2951

Busscher, N., and E. Vojvodić. 2025. "Gas Extraction and Earthquakes in the Netherlands: Drawing Lessons from the Response to Ongoing Social Conflict and Tensions." *Sustainability* 17 (17): 7612. https://doi.org/10.3390/su17177612

Castellazzi, G., A. M. D'Altri, S. de Miranda, and F. Ubertini. 2017. "An Innovative Numerical Modeling Strategy for the Structural Analysis of Historical Monumental Buildings." *Engineering Structures* 132:229–248. https://doi.org/10.1016/j.engstruct.2016.11.032

Chen, X., X. Wang, H. Wang, A. K. Agrawal, A. H. C. Chan, and Y. Cheng. 2021. "Simulating the Failure of Masonry Walls Subjected to Support Settlement With the Combined Finite-Discrete Element Method." *Journal of Building Engineering* 43 (March): 102558. https://doi.org/10.1016/j.jobe.2021.102558

Chen, Z. Q., and T. C. Hutchinson. 2010. "Image-Based Framework for Concrete Surface Crack Monitoring and Quantification." *Advances in Civil Engineering* 2010:1–18. https://doi.org/10.1155/2010/215295

Costa, A. L., S. Kok, and M. Korff. 2020. "Systematic Assessment of Damage to Buildings Due to Groundwater Lowering-Induced Subsidence: Methodology for Large

Scale Application in the Netherlands." In *Proceedings of the International Association of Hydrological Sciences*, Delft-Gouda, The Netherlands, 382, 577–582. https://doi.org/10.5194/piahs-382-577-2020

Dalgic, K. D., B. Gulen, Y. Liu, S. Acikgoz, H. Burd, M. Marasli, and A. Ilki. 2023. "Masonry Buildings Subjected to Settlements: Half-Scale Testing, Detailed Measurements, and Insights into Behaviour." *Engineering Structures* 278:115233. https://doi.org/10.1016/j.engstruct.2022.115233

D'Altri, A. M., S. de Miranda, G. Castellazzi, and V. Sarhosis. 2018. "A 3D Detailed Micro-Model for the In-Plane and Out-of-Plane Numerical Analysis of Masonry Panels." *Computers & Structures* 206:18–30. https://doi.org/10.1016/j.compstruc.2018.06.007

D'Altri, A. M., F. Messali, J. Rots, G. Castellazzi, and S. de Miranda. 2019. "A Damaging Block-Based Model for the Analysis of the Cyclic Behaviour of Full-Scale Masonry Structures." *Engineering Fracture Mechanics* 209:423–448. https://doi.org/10.1016/j.engfracmech.2018.11.046

D'Altri, A. M., M. Pereira, S. de Miranda, and B. Glisic. 2025. "Simulation-Driven Machine Learning for Real-Time Damage Prognosis in Masonry Structures." *International Journal of Mechanical Sciences* 289:110055. https://doi.org/10.1016/j.ijmecsci.2025.110055

D'Altri, A. M., V. Sarhosis, G. Milani, J. Rots, S. Cattari, S. Lagomarsino, E. Sacco, A. Tralli, G. Castellazzi, and S. de Miranda. 2020. "Modeling Strategies for the Computational Analysis of Unreinforced Masonry Structures: Review and Classification." *Archives of Computational Methods in Engineering* 27 (4): 1153–1185. https://doi.org/10.1007/s11831-019-09351-x

D'Ayala, D. F., and S. Paganoni. 2011. "Assessment and Analysis of Damage in L'Aquila Historic City Centre After 6th April 2009." *Bulletin of Earthquake Engineering* 9 (1): 81–104. https://doi.org/10.1007/s10518-010-9224-4

Di Ludovico, M., G. De Martino, A. Prota, G. Manfredi, and M. Dolce. 2021. *Damage Assessment in Italy, and Experiences After Recent Earthquakes on Reparability and Repair Costs*. Cham, Switzerland: Springer Tracts in Civil Engineering. https://doi.org/10.1007/978-3-030-68813-4_4

Dolatshahi, K. M., and A. J. Aref. 2016. "Multi-Directional Response of Unreinforced Masonry Walls: Experimental and Computational Investigations." *Earthquake Engineering and Structural Dynamics* 45 (9): 1427–1449. https://doi.org/10.1002/eqe.2714

Edwards, B., B. Zurek, E. van Dedem, P. J. Stafford, S. Oates, J. van Elk, B. DeMartin, and J. J. Bommer. 2019. "Simulations for the Development of a Ground Motion Model for Induced Seismicity in the Groningen Gas Field, the Netherlands." *Bulletin of Earthquake Engineering* 17 (8): 4441–4456. https://doi.org/10.1007/s10518-018-0479-5

FEMA 306: Evaluation of Earthquake Damaged Concrete and Masonry Wall Buildings. 2000. Vol. 16. Redwood City, CA, USA: Federal Emergency Management Agency. https://doi.org/10.1193/1.1586111

Ferlisi, S., G. Nicodemo, D. Peduto, C. Negulescu, and G. Grandjean. 2020. "Deterministic and Probabilistic Analyses of the 3D Response of Masonry Buildings to Imposed Settlement Troughs." *Georisk: Assessment and Management of Risk for Engineered Systems and Geohazards* 14 (4): 260–279. https://doi.org/10.1080/17499518.2019.1658880

Franza, A., S. Miraei, D. Boldini, and N. Losacco. 2022. "An Equivalent Beam Approach for Assessing Tunnelling-Induced Distortions of Frames with Infills." *Tunnelling and Underground Space Technology* 129:104686. https://doi.org/10.1016/j.tust.2022.104686

Furiosi, A., N. Damiani, M. Rota, and A. Penna. 2025. "Seismic Fragility Assessment of a Multi-Span Masonry Arch Bridge Using a Discontinuum Modeling Approach." *Earthquake Engineering and Structural Dynamics* 54 (13): 3320–3340. https://doi.org/10.1002/eqe.70029

Furtado, A., H. Rodrigues, A. Arêde, and H. Varum. 2018. "Out-of-Plane Behavior of Masonry Infilled RC Frames Based on the Experimental Tests Available: A Systematic Review." *Construction and Building Materials* 168:831–848. https://doi.org/10.1016/j.conbuildmat.2018.02.129

Gagliardo, R., F. P. A. Portioli, L. Cascini, R. Landolfo, and P. B. Lourenço. 2021. "A Rigid Block Model with No-Tension Elastic Contacts for Displacement-Based Assessment of Historic Masonry Structures Subjected to Settlements." *Engineering Structures* 229:111609. https://doi.org/10.1016/j.engstruct.2020.111609

Gentile, R., G. Cremen, C. Galasso, L. T. Jenkins, V. Manandhar, E. Y. Menteşe, R. Guragain, and J. McCloskey. 2022. "Scoring, Selecting, and Developing Physical Impact Models for Multi-Hazard Risk Assessment." *International Journal of Disaster Risk Reduction* 82:103365. https://doi.org/10.1016/j.ijdrr.2022.103365

Ghezelbash, A., A. Aşıkoğlu, A. M. D'Altri, S. Sharma, and F. Messali. 2025. "Blind Prediction of the Dynamic Behavior of 3D-Printed Masonry-Like Structures Under Shake-Table Loading via a High-Fidelity Numerical Modeling Approach (Under Review)." *Results in Engineering* 25. https://doi.org/10.1016/j.rineng.2024.103755

Ghezelbash, A., A. Aşıkoğlu, A. M. D'Altri, S. Sharma, and F. Messali. 2026. "High-Fidelity Numerical Modeling of the Dynamic Behavior of 3D-Printed Masonry-Like Sub-Structures Under Shake-Table Loading." In *10th European Congress on Computational Methods in Applied Sciences and Engineering (ECCOMAS)*, 55. Munich, Germany: International Association for Computational Mechanics.

Ghezelbash, A., A. M. D'Altri, P. B. Lourenço, and S. de Miranda. 2026. "Numerical Modeling of the Out-of-Plane Dynamic Response of Masonry Gable Walls via a High-Fidelity Block-Based Finite Element Modeling Approach – Part I: Blind Prediction." *Bulletin of Earthquake Engineering*. https://doi.org/10.1007/s10518-025-02328-1

Ghezelbash, A., A. M. D'Altri, S. Sharma, P. B. Lourenço, J. G. Rots, and F. Messali. 2025. "A Block-Based Numerical Strategy for Modeling the Dynamic Out-of-Plane Behavior of Unreinforced Brick Masonry Walls." *Meccanica* 60 (7): 2069–2105. https://doi.org/10.1007/s11012-024-01899-8

Ghezelbash, A., F. Messali, D. Am, and J. G. Rots. 2024. "Challenges in the Dynamic Analysis of Masonry Walls Using Block-Based Finite Element Interface Models." In *9th European Congress on Computational Methods in*

Applied Sciences and Engineering (ECCOMAS), 432. Lisbon, Portugal: International Association for Computational Mechanics.

Ghezelbash, A., F. Messali, and J. G. Rots. 2023a. "Challenges in the Calibration of Finite Element Models for the Analysis of Masonry Structures: A Comparative Study." In *XVII International Conference on Computational Plasticity, Fundamentals and Applications*. Barcelona, Spain: International Centre for Numerical Methods in Engineering.

Ghezelbash, A., F. Messali, and J. G. Rots. 2023b. "Finite Element Micro-Modelling of Masonry Structures: Calibration and Analysis Challenges." In *Engineering Mechanics Institute (EMI) International Conference*. Palermo, Italy: Engineering Mechanics Institute.

Ghezelbash, A., J. G. Rots, and F. Messali. 2025. "Review of the Influence of the Interaction Between In-Plane and Out-of-Plane Behaviors on the Seismic Response of Non-Framed Unreinforced Masonry Walls." *Buildings* 15 (16): 2874. https://doi.org/10.3390/buildings15162874

Ghezelbash, A., S. Sharma, A. M. D'Altri, P. B. Lourenço, J. G. Rots, and F. Messali. 2025. "Challenges in High-Fidelity Implicit Block-Based Numerical Simulation of Dynamic Out-of-Plane Two-Way Bending in Unreinforced Brick Masonry Walls." *Earthquake Engineering and Structural Dynamics* 54 (7): 1836–1858. https://doi.org/10.1002/eqe.4337

Ghezelbash, A., S. Sharma, J. G. Rots, and F. Messali. 2025. "Effect of Relative Support Motions on the Out-of-Plane Dynamics of One-Way Spanning Unreinforced Masonry Walls and Insights into Their Instability Displacement." *Journal of Structural Engineering* https://doi.org/10.1061/JSENDH/STENG-15104.

Giardina, G. 2013. *Modelling of Settlement Induced Building Damage*. Delft, The Netherlands: Delft University of Technology.

Giardina, G., A. Marini, M. A. N. Hendriks, J. G. Rots, F. Rizzardini, and E. Giuriani. 2012. "Experimental Analysis of a Masonry Façade Subject to Tunnelling-Induced Settlement." *Engineering Structures* 45:421–434. https://doi.org/10.1016/j.engstruct.2012.06.042

Giardina, G., A. Marini, P. Riva, and E. Giuriani. 2020. "Analysis of a Scaled Stone Masonry Facade Subjected to Differential Settlements." *International Journal of Architectural Heritage* 14 (10): 1502–1516. https://doi.org/10.1080/15583058.2019.1617911

Giardina, G., A. V. van de Graaf, M. A. N. Hendriks, J. G. Rots, and A. Marini. 2013. "Numerical Analysis of a Masonry Façade Subject to Tunnelling-Induced Settlements." *Engineering Structures* 54:234–247. https://doi.org/10.1016/j.engstruct.2013.03.055

Godio, M., and K. Beyer. 2019. "Quantifying the Out-of-Plane Response of Unreinforced Masonry Walls Subjected to Relative Support Motion." *Frattura ed Integrità Strutturale* 13 (50): 194–208. https://doi.org/10.3221/IGF-ESIS.50.17

Graziotti, F., U. Tomassetti, S. Kallioras, A. Penna, and G. Magenes. 2017. "Shaking Table Test on a Full Scale URM Cavity Wall Building." *Bulletin of Earthquake Engineering* 15 (12): 5329–5364. https://doi.org/10.1007/s10518-017-0185-8

Graziotti, F., U. Tomassetti, S. Sharma, L. Grottoli, and G. Magenes. 2019. "Experimental Response of URM Single Leaf and Cavity Walls in Out-of-Plane Two-Way Bending Generated by Seismic Excitation." *Construction and Building Materials* 195:650–670. https://doi.org/10.1016/j.conbuildmat.2018.10.076

Grünthal, G. 1998. *EMS-98: European Macroseismic Scale*. Luxembourg: European Seismological Commission.

Hendry, E. A. W. 2001. "Masonry Walls: Materials and Construction." *Construction and Building Materials* 15 (8): 323–330. https://doi.org/10.1016/S0950-0618(01)00019-8

Hibbitt, D., B. Karlsson, and P. Sorensen. 2011. *Abaqus/CAE User's Manual*. USA: Dassault Systèmes SE.

Hilber, H. M., T. J. Hughes, and R. L. Talor. 1977. "Improved Numerical Dissipation for Time Integration Algorithms in Structural Dynamics." *Earthquake Engineering and Structural Dynamics* 5 (3): 282–292. https://doi.org/10.1002/eqe.4290050306

Hong, L. T., and D. F. Laefer. 2008. "Micro vs. Macro Models for Predicting Building Damage Underground Movements." In *The international Conference on Computational Solid Mechanics*. Hochiminh City, Vietnam: Vietnam Association for Mechanics of Solid.

Itasca. 2020. *3DEC — Three-Dimensional Distinct Element Code, Version 7.0*. Minneapolis, MN, USA: Itasca Consulting Group, Inc.

Jafari, S. 2021. *Material Characterisation of Existing Masonry: A Strategy to Determine Strength, Stiffness and Toughness Properties for Structural Analysis*. Delft, Netherlands: Delft University of Technology.

Jafari, S., and R. Esposito. 2016. *Material Tests for the Characterisation of Replicated Calcium Silicate Brick Masonry*. Delft, Netherlands: Delft University of Technology.

Jafari, S., R. Esposito, and J. G. Rots. 2019. "From Brick to Element: Investigating the Mechanical Properties of Calcium Silicate Masonry." In *Structural Analysis of Historical Constructions*, 596–604. Cusco, Perú. https://doi.org/10.1007/978-3-319-99441-3_64.

Karanikoloudis, G., J. Serra, and P. B. Lourenço. 2024. "Experimental Tests and Analytical Strength Models of Differential Settlements on Unreinforced Masonry Piers and Spandrel Specimens." *Journal of Building Engineering* 89:109192. https://doi.org/10.1016/j.jobe.2024.109192

Kesavan, P., and A. Menon. 2022. "Investigation of In-Plane and Out-of-Plane Interaction in Unreinforced Masonry Piers by Block-Based Micro-Modeling." *Structures* 46:1327–1344. https://doi.org/10.1016/j.istruc.2022.10.105

KNMI (Royal Netherlands Meteorological Institute). "Aardbevingen Door Gaswinning." Accessed August 12, 2025. https://www.knmi.nl/kennis-en-datacentrum/uitleg/aardbevingen-door-gaswinning.

Koc, A. B., M. A. Erberik, A. Askan, and S. Karimzadeh. 2023. "The Sensitivity of Global Structural Parameters for Unreinforced Masonry Buildings Subjected to Simulated Ground Motions." *Buildings* 13 (8): 2060. https://doi.org/10.3390/buildings13082060

Korany, Y., R. Drysdale, and S. Chidiac. 2001. "Retrofit of Unreinforced Masonry Buildings: The State-of-the-Art." 9th Canadian Masonry Symposium, Fredericton, Canada.

Korswagen, P. A. 2024. "Quantifying the Probability of Light Damage to Masonry Structures: An Exploration of Crack Initiation and Progression Due to Seismic Vibrations on

Masonry Buildings with Existing Damage." PhD Thesis, Delft, The Netherlands: Delft University of Technology.
Korswagen, P. A., M. Longo, A. Prosperi, J. G. Rots, and K. C. Terwel. 2024. "Modelling of Damage in Historical Masonry Façades Subjected to a Combination of Ground Settlement and Vibrations." In *Structural Analysis of Historical Constructions*, 904–917. Cham, Germany: Springer Nature. https://doi.org/10.1007/978-3-031-39603-8_73
Koster, K., J. Stafleu, and E. Stouthamer. 2018. "Differential Subsidence in the Urbanised Coastal-Deltaic Plain of the Netherlands." *Netherlands Journal of Geosciences* 97 (4): 215–227. https://doi.org/10.1017/njg.2018.11
Lee, J., and G. L. Fenves. 1998. "Plastic-Damage Model for Cyclic Loading of Concrete Structures." *Journal of Engineering Mechanics* 124 (8): 892–900. https://doi.org/10.1061/(ASCE)0733-9399(1998)124:8(892)
Longo, M., M. Sousamli, P. A. Korswagen, P. van Staalduinen, and J. G. Rots. 2021. "Sub-Structure-Based 'Three-Tiered' Finite Element Approach to Soil-Masonry-Wall Interaction for Light Seismic Motion." *Engineering Structures* 245:112847. https://doi.org/10.1016/j.engstruct.2021.112847
Lubliner, J., J. Oliver, S. Oller, and E. Oñate. 1989. "A Plastic-Damage Model for Concrete." *International Journal of Solids and Structures* 25 (3): 299–326. https://doi.org/10.1016/0020-7683(89)90050-4
2016. *Maatschappelijke Effecten Inventarisatie van Aardbevingen in Noordoost Groningen*. Amersfoort, Netherlands: Royal Haskoning DHV.
Macorini, L., and B. A. Izzuddin. 2011. "A Non-Linear Interface Element for 3D Mesoscale Analysis of Brick-Masonry Structures." *International Journal for Numerical Methods in Engineering* 85 (12): 1584–1608. https://doi.org/10.1002/nme.3046
Malomo, D., R. Pinho, and A. Penna. 2020. "Numerical Modelling of the Out-of-Plane Response of Full-Scale Brick Masonry Prototypes Subjected to Incremental Dynamic Shake-Table Tests." *Engineering Structures* 209:110298. https://doi.org/10.1016/j.engstruct.2020.110298
Meoni, A., M. Mattiacci, A. D'Alessandro, G. Virgulto, N. Buratti, and F. Ubertini. 2025. "Automated Damage Detection in Masonry Structures Using Cointegrated Strain Measurements from Smart Bricks: Application to a Full-Scale Building Model Subjected to Foundation Settlements Under Changing Environmental Conditions." *Journal of Building Engineering* 100:111749. https://doi.org/10.1016/j.jobe.2024.111749
Messali, F., R. Esposito, G. J. P. Ravenshorst, and J. G. Rots. 2020. "Experimental Investigation of the In-Plane Cyclic Behaviour of Calcium Silicate Brick Masonry Walls." *Bulletin of Earthquake Engineering* 18 (8): 3963–3994. https://doi.org/10.1007/s10518-020-00835-x.
Messali, F., J. Rots, and J. Walraven. 2020. *Backgrounds NPR 9998:2018 Annex G*. Delft, Netherlands: Nederlandse Normalisatie Instituut.
Miglietta, M., N. Damiani, G. Guerrini, and F. Graziotti. 2021. "Full-Scale Shake-Table Tests on Two Unreinforced Masonry Cavity-Wall Buildings: Effect of an Innovative Timber Retrofit." *Bulletin of Earthquake Engineering* 19 (6): 2561–2596. https://doi.org/10.1007/s10518-021-01057-5
Milani, G., M. Valente, and C. Alessandri. 2018. "The Narthex of the Church of the Nativity in Bethlehem: A Non-Linear Finite Element Approach to Predict the Structural Damage." *Computers & Structures* 207:3–18. https://doi.org/10.1016/j.compstruc.2017.03.010
Mirmiran, A., and M. Shahawy. 1997. "Dilation Characteristics of Confined Concrete." *Mechanics of Cohesive-Frictional Materials* 2 (3): 237–249. https://doi.org/10.1002/(SICI)1099-1484(199707)2:3<237:AID-CFM32>3.0.CO;2-2
Mohyeddin, A., H. M. Goldsworthy, and E. F. Gad. 2013. "FE Modelling of RC Frames with Masonry Infill Panels Under In-Plane and Out-of-Plane Loading." *Engineering Structures* 51:73–87. https://doi.org/10.1016/j.engstruct.2013.01.012
Moon, L., D. Dizhur, I. Senaldi, H. Derakhshan, M. Griffith, G. Magenes, and J. Ingham. 2014. "The Demise of the URM Building Stock in Christchurch During the 2010–2011 Canterbury Earthquake Sequence." *Earthquake Spectra* 30 (1): 253–276. https://doi.org/10.1193/022113EQS044M
Napolitano, R., and B. Glisic. 2019. "Methodology for Diagnosing Crack Patterns in Masonry Structures Using Photogrammetry and Distinct Element Modeling." *Engineering Structures* 181:519–528. https://doi.org/10.1016/j.engstruct.2018.12.036
Netzel, H. D. 2009. *Building Response Due to Ground Movements*. Delft, The Netherlands: Delft University of Technology.
Nicodemo, G., D. Peduto, and S. Ferlisi. 2019. "Numerical Analysis of the Behaviour of Masonry Buildings Undergoing Differential Settlements." In *17th European Conference on Soil Mechanics and Geotechnical Engineering*, 1–8. Reykjavik, Iceland: International Society for Soil Mechanics and Geotechnical Engineering.
Nicodemo, G., D. Peduto, and S. Ferlisi. 2020. "Building Damage Assessment and Settlement Monitoring in Subsidence-Affected Urban Areas: Case Study in the Netherlands." In *Proceedings of the International Association of Hydrological Sciences*, International Association of Hydrological Sciences. 382, 651–656. https://doi.org/10.5194/piahs-382-651-2020
Nie, Y., A. Sheikh, P. Visintin, and M. Griffith. 2023. "A Robust Computational Strategy for Failure Prediction of Masonry Structures Using an Improved Multi-Surface Damage-Plastic Based Interface Model." *International Journal for Numerical Methods in Engineering* 124 (11): 2498–2528. https://doi.org/10.1002/nme.7218
Nieuwenhuis, H. S., and F. Schokking. 1997. "Land Subsidence in Drained Peat Areas of the Province of Friesland, the Netherlands." *Quarterly Journal of Engineering Geology* 30 (1): 37–48. https://doi.org/10.1144/GSL.QJEGH.1997.030.P1.04
Oktiovan, Y. P., L. Davis, R. Wilson, A. Dell'endice, A. Mehrotra, B. Pulatsu, and D. Malomo. 2024. "Simplified Micro-Modeling of a Masonry Cross-Vault for Seismic Assessment Using the Distinct Element Method." *International Journal of Architectural Heritage* 18 (12): 1915–1948. https://doi.org/10.1080/15583058.2023.2277328
Oktiovan, Y. P., F. Messali, B. Pulatsu, J. V. Lemos, and J. G. Rots. 2024. "A Contact-Based Constitutive Model for

the Numerical Analysis of Masonry Structures Using the Distinct Element Method." *Computers & Structures* 303:107499. https://doi.org/10.1016/j.compstruc.2024.107499

Oyarzo-Vera, C., and M. C. Griffith. 2009. "The Mw 6.3 Abruzzo (Italy) Earthquake of April 6th, 2009: On Site Observations." *Bulletin of the New Zealand Society for Earthquake Engineering* 42 (4): 302–307. https://doi.org/10.5459/bnzsee.42.4.302-307

Page, A. W. 1991. "The Newcastle Earthquake - Behaviour of Masonry Structures." *Masonry International* 5:11–18.

Patel, K. P., and R. N. Dubey. 2022. "Effect of Flanges on the In-Plane Behavior of the Masonry Walls." *Engineering Structures* 273:115059. https://doi.org/10.1016/j.engstruct.2022.115059

Patel, K. P., and R. N. Dubey. 2023. "Effect of Cross Walls on the Interaction Curves of the Unreinforced Masonry Walls." *Earthquake Engineering and Structural Dynamics* 52 (14): 4518–4545. https://doi.org/10.1002/eqe.3967

Peck, R. B. 1969. "Deep Excavations and Tunneling in Soft Ground." In *7th International Conference on Soil Mechanics and Foundation Engineering*, 225–290. Mexico, Mexico: International Society for Soil Mechanics and Geotechnical Engineering.

Peduto, D., S. Ferlisi, G. Nicodemo, D. Reale, G. Pisciotta, and G. Gullà. 2017. "Empirical Fragility and Vulnerability Curves for Buildings Exposed to Slow-Moving Landslides at Medium and Large Scales." *Landslides* 14 (6): 1993–2007. https://doi.org/10.1007/s10346-017-0826-7

Peduto, D., M. Korff, G. Nicodemo, A. Marchese, and S. Ferlisi. 2019. "Empirical Fragility Curves for Settlement-Affected Buildings: Analysis of Different Intensity Parameters for Seven Hundred Masonry Buildings in the Netherlands." *Soils and Foundations* 59 (2): 380–397. https://doi.org/10.1016/j.sandf.2018.12.009

Peduto, D., G. Nicodemo, J. Maccabiani, and S. Ferlisi. 2017. "Multi-Scale Analysis of Settlement-Induced Building Damage Using Damage Surveys and DInSAR Data: A Case Study in the Netherlands." *Engineering Geology* 218:117–133. https://doi.org/10.1016/j.enggeo.2016.12.018

Peduto, D., G. Nicodemo, J. Maccabiani, S. Ferlisi, R. D'Angelo, and A. Marchese. 2016. "Investigating the Behaviour of Buildings with Different Foundation Types on Soft Soils: Two Case Studies in the Netherlands." *Procedia Engineering* 158:529–534. https://doi.org/10.1016/j.proeng.2016.08.484

Peduto, D., A. Prosperi, G. Nicodemo, and M. Korff. 2022. "District-Scale Numerical Analysis of Settlements Related to Groundwater Lowering in Variable Soil Conditions." *Canadian Geotechnical Journal* 59 (6): 978–993. https://doi.org/10.1139/cgj-2021-0041

Penna, A., P. Morandi, M. Rota, C. F. Manzini, F. da Porto, and G. Magenes. 2014. "Performance of Masonry Buildings During the Emilia 2012 Earthquake." *Bulletin of Earthquake Engineering* 12 (5): 2255–2273. https://doi.org/10.1007/s10518-013-9496-6

Portioli, F., and L. Cascini. 2017. "Large Displacement Analysis of Dry-Jointed Masonry Structures Subjected to Settlements Using Rigid Block Modelling." *Engineering Structures* 148:485–496. https://doi.org/10.1016/j.engstruct.2017.06.073

Portioli, F. P. A., L. Cascini, R. Landolfo, and P. B. Lourenço. 2023. "An Optimization-Based Rigid Block Modeling Approach to Seismic Assessment of Dry-Joint Masonry Structures Subjected to Settlements." *Soil Dynamics and Earthquake Engineering* 166:107760. https://doi.org/10.1016/j.soildyn.2023.107760

Pradhan, B., M. Zizzo, V. Sarhosis, and L. Cavaleri. 2021. "Out-of-Plane Behaviour of Unreinforced Masonry Infill Walls: Review of the Experimental Studies and Analysis of the Influencing Parameters." *Structures* 33:4387–4406. https://doi.org/10.1016/j.istruc.2021.07.038

Prosperi, A. 2025. "Modelling of Subsidence Induced Damage to Masonry Buildings: Influence of Soil Heterogeneity on Settlement and Development of Fragility." PhD Thesis, Delft, The Netherlands: Delft University of Technology.

Prosperi, A., P. A. Korswagen, M. Korff, R. Schipper, and J. G. Rots. 2023. "Empirical Fragility and ROC Curves for Masonry Buildings Subjected to Settlements." *Journal of Building Engineering* 68:106094. https://doi.org/10.1016/j.jobe.2023.106094

Prosperi, A., P. A. Korswagen, M. Longo, M. Korff, and J. G. Rots. 2025. "Toward NLFEA-Based Fragility Curves for Unreinforced Masonry Buildings Exposed to Subsidence." *Journal of Building Engineering* 112:113676. https://doi.org/10.1016/j.jobe.2025.113676

Prosperi, A., M. Longo, P. A. Korswagen, M. Korff, and J. G. Rots. 2023a. "Accurate and Efficient 2D Modelling of Historical Masonry Buildings Subjected to Settlements in Comparison to 3D Approaches." In *International Conference on Structural Analysis of Historical Constructions*, edited by Y. Endo and T. Hanazato, 232–244. Kyoto, Japan: Springer Nature.

Prosperi, A., M. Longo, P. A. Korswagen, M. Korff, and J. G. Rots. 2023b. "Sensitivity Modelling with Objective Damage Assessment of Unreinforced Masonry Façades Undergoing Different Subsidence Settlement Patterns." *Engineering Structures* 286:116113. https://doi.org/10.1016/j.engstruct.2023.116113

Prosperi, A., M. Longo, P. A. Korswagen, M. Korff, and J. G. Rots. 2025. "2D and 3D Modelling Strategies to Reproduce the Response of Historical Masonry Buildings Subjected to Settlements." *International Journal of Architectural Heritage* 19 (5): 1–17. https://doi.org/10.1080/15583058.2024.2325472

Rots, J. G., P. A. Korswagen, and M. Longo. 2021. *Computational Modelling Checks of Masonry Building Damage Due to Deep Subsidence*. Delft, The Netherlands: Delft University of Technology.

Saeidi, A., O. Deck, and T. Verdel. 2009. "Development of Building Vulnerability Functions in Subsidence Regions from Empirical Methods." *Engineering Structures* 31 (10): 2275–2286. https://doi.org/10.1016/j.engstruct.2009.04.010

Scacco, J., B. Ghiassi, G. Milani, and P. B. Lourenço. 2020. "A Fast Modeling Approach for Numerical Analysis of Unreinforced and FRCM Reinforced Masonry Walls Under Out-of-Plane Loading." *Composites Part B Engineering* 180:107553. https://doi.org/10.1016/j.compositesb.2019.107553

Sharma, S., N. Damiani, M. Bertassi, M. Smerilli, M. Mirra, I. Lanese, E. R. Parisi, G. J. O'Reilly, F. Messali, and

F. Graziotti. 2025. "Experimental Data from Out-of-Plane Shake-Table Tests on Unreinforced Masonry Gables." *Earthquake Spectra* 41 (5): 4227–4245. https://doi.org/10.1177/87552930251378248

Sharma, S., L. C. Silva, F. Graziotti, G. Magenes, and G. Milani. 2021. "Modelling the Experimental Seismic Out-of-Plane Two-Way Bending Response of Unreinforced Periodic Masonry Panels Using a Non-linear Discrete Homogenized Strategy." *Engineering Structures* 242:112524. https://doi.org/10.1016/j.engstruct.2021.112524

Sharma, S., U. Tomassetti, L. Grottoli, and F. Graziotti. 2020. "Two-Way Bending Experimental Response of URM Walls Subjected to Combined Horizontal and Vertical Seismic Excitation." *Engineering Structures* 219:110537. https://doi.org/10.1016/j.engstruct.2020.110537

Son, M., and E. J. Cording. 2005. "Estimation of Building Damage Due to Excavation-Induced Ground Movements." *Journal of Geotechnical and Geoenvironmental Engineering* 131 (2): 162–177. https://doi.org/10.1061/(ASCE)1090-0241(2005)131:2(162)

Son, M., and E. J. Cording. 2007. "Evaluation of Building Stiffness for Building Response Analysis to Excavation-Induced Ground Movements." *Journal of Geotechnical and Geoenvironmental Engineering* 133 (8): 995–1002. https://doi.org/10.1061/(ASCE)1090-0241(2007)133:8(995)

Soundar Rajan, M., and D. Jegatheeswaran. 2023. "Influence of Strength Behavior in Brick Masonry Prism and Wallette Under Compression." *Matéria (Rio De Janeiro)* 28 (1). https://doi.org/10.1590/1517-7076-rmat-2022-0260

Stouthamer, E., G. Erkens, K. Cohen, D. Hegger, P. Driessen, H. P. Weikard. 2020. "Dutch National Scientific Research Program on Land Subsidence: Living on Soft Soils – Subsidence and Society." In *Proceedings of the International Association of Hydrological Sciences*. Delft-Gouda, The Netherlands: International Association of Hydrological Sciences. 382, 815–819. https://doi.org/10.5194/piahs-382-815-2020

Taucer, F., and A. Pinto Vieira. 2007. "EUR 22868 EN: Field Manual for Post-Earthquake Damage and Safety Assessment and Short Term Countermeasures (AeDES)."

Tomassetti, U., A. A. Correia, P. X. Candeias, F. Graziotti, and A. Campos Costa. 2019. "Two-Way Bending Out-of-Plane Collapse of a Full-Scale URM Building Tested on a Shake Table." *Bulletin of Earthquake Engineering* 17 (4): 2165–2198. https://doi.org/10.1007/s10518-018-0507-5

U.S. Geological Survey. M 6.9. 2019. *Loma Prieta Earthquake*.

van Asselen, S., G. Erkens, E. Stouthamer, H. A. G. Woolderink, R. E. E. Geeraert, and M. M. Hefting. 2018. "The Relative Contribution of Peat Compaction and Oxidation to Subsidence in Built-Up Areas in the Rhine-Meuse Delta, the Netherlands." *Science of the Total Environment* 636:177–191. https://doi.org/10.1016/j.scitotenv.2018.04.141

van Staalduinen PC, K. Terwel, and J. G. Rots. 2018. *Onderzoek Naar de Oorzaken van Bouwkundige Schade in Groningen Methodologie en Case Studies ter Duiding van de Oorzaken*. Delft, Netherlands: Faculty of Civil Engineering and Geosciences, Delft University of Technology.

Wang, J., W. Hu, X. Wang, and Y. Liang. 2021. "Experimental Investigation of Crack Initiation and Propagation in the Unreinforced Masonry Specimen Subjected to Vertical Settlement." *Advances in Materials Science and Engineering* 2021 (1). https://doi.org/10.1155/2021/6672037

Weyler, R., J. Oliver, T. Sain, and J. C. Cante. 2012. "On the Contact Domain Method: A Comparison of Penalty and Lagrange Multiplier Implementations." *Computer Methods in Applied Mechanics and Engineering* 205–208:68–82. https://doi.org/10.1016/j.cma.2011.01.011

Xie, Z., M. Sousamli, F. Messali, and J. G. Rots. 2021. "A Sub-stepping Iterative Constitutive Model for Cyclic Cracking-Crushing-Shearing in Masonry Interface Elements." *Computers & Structures* 257:106654. https://doi.org/10.1016/j.compstruc.2021.106654

Yiu, W. N., H. J. Burd, and C. M. Martin. 2018. "Finite-Element Modelling for the Assessment of Tunnel-Induced Damage to a Masonry Building." *Géotechnique* 67 (9): 780–794. https://doi.org/10.1680/tue.63778.059.

Zhao, J., and M. DeJong. 2023. "Three-Dimensional Probabilistic Assessment of Tunneling Induced Structural Damage Using Monte-Carlo Method and Hybrid Finite Element Model." *Computers and Geotechnics* 154:105122. https://doi.org/10.1016/j.compgeo.2022.105122